

Quarterly Technical Report

Solid State Research


2004:3

Lincoln Laboratory
MASSACHUSETTS INSTITUTE OF TECHNOLOGY
LEXINGTON, MASSACHUSETTS



Prepared for the Department of the Air Force under Contract F19628-00-C-0002.

Approved for public release; distribution is unlimited.



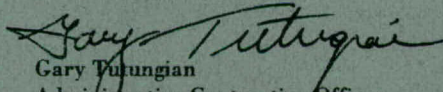
This report is based on studies performed at Lincoln Laboratory, a center for research operated by Massachusetts Institute of Technology. This work was sponsored by the Department of the Air Force under Contract F19628-00-C-0002.

This report may be reproduced to satisfy needs of U.S. Government agencies.

The ESC Public Affairs Office has reviewed this report, and it is releasable to the National Technical Information Service, where it will be available to the general public, including foreign nationals.

This technical report has been reviewed and is approved for publication.

FOR THE COMMANDER


Gary Tutungian
Administrative Contracting Officer
Plans and Programs Directorate
Contracted Support Management

Non-Lincoln Recipients

PLEASE DO NOT RETURN

Permission is given to destroy this document
when it is no longer needed.

**Massachusetts Institute of Technology
Lincoln Laboratory**

Solid State Research

**Quarterly Technical Report
2004:3**

1 May – 31 July 2004

Issued 20 December 2004

Approved for public release; distribution is unlimited.

Lexington

Massachusetts

ABSTRACT

This report covers in detail the research work of the Solid State Division at Lincoln Laboratory for the period 1 May through 31 July 2004. The topics covered are Quantum Electronics, Electro-optical Materials and Devices, Submicrometer Technology, Biosensor and Molecular Technologies, Advanced Imaging Technology, Analog Device Technology, and Advanced Silicon Technology. Funding is provided by several DoD organizations—including the Air Force, Army, DARPA, MDA, Navy, NSA, and OSD—and also by the DOE, NASA, and NIST.

TABLE OF CONTENTS

Abstract	iii
List of Illustrations	vii
List of Tables	x
Introduction	xi
Reports on Solid State Research	xiii
Organization	xxv
 1. QUANTUM ELECTRONICS	
1.1 120-W Cryogenically Cooled Yb:YAG Laser	1
 2. ELECTRO-OPTICAL MATERIALS AND DEVICES	
2.1 Antimonide-Based Avalanche Photodiodes for the Mid-IR	5
2.2 OMVPE Growth of InGaAsP/InP	8
 3. SUBMICROMETER TECHNOLOGY	
3.1 Nanocomposite Approaches Toward Pellicles for 157-nm Lithography	11
 4. BIOSENSOR AND MOLECULAR TECHNOLOGIES	
4.1 Compatibility Testing of LiNK 2.0 with RAZOR	17
 5. ADVANCED IMAGING TECHNOLOGY	
5.1 Orthogonal-Transfer Array for Adaptive Imaging in Astronomy	23
 6. ANALOG DEVICE TECHNOLOGY	
6.1 Electromagnetically Induced Transparency with Superconductive Quantum Circuits	27

7. ADVANCED SILICON TECHNOLOGY

7.1 High-Speed Schottky Barrier pMOSFET with $f_T = 280$ GHz

35

LIST OF ILLUSTRATIONS

Figure No.		Page
1-1	Thermal conductivity κ ; coefficient of thermal expansion α , and thermo-optic coefficient dn/dT of YAG measured from 100 K to room temperature.	1
1-2	Schematic of diode end-pumped cryogenically cooled Yb:YAG laser.	2
1-3	(a) Output power of cryogenically cooled Yb:YAG laser as a function of incident diode pump power, and (b) beam profile at 60-W output power.	2
2-1	Scanning electron micrographs of (a) etched device mesa, and (b) passivated 30- μm -diameter devices with annular contacts and bond pads.	6
2-2	Current vs voltage characteristic of 30- μm -diameter separate-absorber-multiplier avalanche photodiode operated at 77 K. The photocurrent vs voltage characteristic was measured simultaneously while illuminating the device with a chopped 3.39- μm optical source.	7
2-3	Dark count rate vs overbias for a 41% AlGaAsSb PIN diode operating in the Geiger mode. The breakdown voltage at 290 K is 29.91 V and at 77 K is 26.62 V.	7
2-4	Curves summarizing the group V vapor-solid data, with $y(v)$ the As fraction in the vapor and $y(s)$ that in the solid. The lower curve fits the close-coupled showerhead (CCS) reactor data well, and the upper curve represents the lower limit of scattered data for the chimney reactor. The comparison shows the greater accessibility to low $y(s)$ values in the CCS reactor.	9
3-1	Refractive index at 414 nm as a function of nanoparticle loading. Three curves are shown: bare nanoparticles (ST-S) as well as two surface modifications: short chain (SC) at 25% surface loading and long chain (LC) at 2.5% surface loading. Also, a linear fit to the ST-S data is shown (dashed line), based on a prediction from effective medium approximation, as described in the text.	12
3-2	Transmission for 1- μm -thick 2P films spun cast on CaF_2 substrates. The trace labels refer to either a neat polymer ("neat") or to a polymer loaded with ST-S nanoparticles with the weight percent as indicated.	13
3-3	157-nm transmission loss for bare nanoparticles and two different surface terminations.	13

LIST OF ILLUSTRATIONS (Continued)

Figure No.		Page
3-4	157-nm induced absorbance in several laser-irradiated polymer films, both neat and ST-S loaded polymer.	14
3-5	157-nm induced absorbance in several laser-irradiated polymer films, both neat and SC-loaded polymer.	15
4-1	Results of assay for Ba spore in dirty water.	18
4-2	Results of assay for Btk spore in dirty water.	18
4-3	Results of assay for Ba spore in Leighton-Doi growth media: (a) pXO1 target and (b) chromosomal target (RAZOR data only).	19
4-4	Results of assay for Btk spore in Leighton-Doi growth media.	19
4-5	Results of assay for Ba spore in sand.	20
4-6	Results of assay for Btk spore in sand.	20
4-7	Comparison between ABI 7700 + SNAP and RAZOR + LiNK 2.0 for detection of (a) Ba spore at 1×10^3 cfu/mL and (b) Btk spore at 1×10^3 cfu/mL.	21
5-1	Principal elements of the orthogonal transfer array (OTA): (a) Overall chip layout comprising an 8×8 array of OTCCD cells, (b) OTA cell with its control logic, and (c) one of the OTCCD pixel geometries.	23
5-2	Depiction of OTA operation.	24
5-3	Arrangement of control lines and logic for each OTA cell.	25
5-4	Photograph of completed wafer showing four large OTAs surrounded by smaller versions of OTAs (2×2 cells), a standard three-phase imager, and process control cells.	26

LIST OF ILLUSTRATIONS (Continued)

Figure No.		Page
6-1	<p>(a) Atomic Λ-system. Levels 1 and 2 are taken to be metastable, and level 3 decays primarily to levels outside the system at a rate Γ_3. ω_i are the frequencies of the levels (energy in rad/sec). Ω_{ij} are the Rabi frequencies used to represent the field strengths of the driven transitions. (b) Radiation drives the $1 \rightarrow 3$ transition. Population in level 1 is transferred to level 3 by the absorption of photons, where it is assumed to decay via the Γ_3 channels. (c) Radiation drives the $2 \rightarrow 3$ transition. Population in level 2 is transferred to level 3 by the absorption of photons, where it is assumed to decay via the Γ_3 channels. (d) If the system is prepared in a dark state, the simultaneous application of radiation fields Ω_{13} and Ω_{23} results in electromagnetically induced transparency; no photon absorption occurs owing to a destructive quantum interference of the two driven transitions. As a result, population remains in the dark state (levels 1 and 2).</p>	28
6-2	<p>(a) Superconductive flux qubit and superconducting quantum interference device (SQUID). φ_1 and φ_2 are the gauge-invariant phases of the larger-two qubit junctions. An applied flux f tunes the potential landscape of the qubit. (b) Asymmetric double-well potential of the flux qubit at a bias point $f = 0.504$. The three levels in the left well constitute the Λ-system. Tunneling to the right well can be observed by the SQUID. (c) Microwave radiation drives the $1 \rightarrow 3$ transition. Population in level 1 is transferred to level 3 by the absorption of photons, where it quickly tunnels to the right well and is detected by the SQUID. (d) Microwave radiation drives the $2 \rightarrow 3$ transition. Population in level 2 is transferred to level 3 by the absorption of photons, where it quickly tunnels to the right well and is detected by the SQUID. (e) If the qubit is prepared in a dark state, the simultaneous application of microwave fields Ω_{13} and Ω_{23} results in EIT; no photon absorption occurs because of a destructive quantum interference of the two driven transitions. As a result, population remains in the dark state (levels 1 and 2). Since no population reaches state $3\rangle$, the SQUID does not detect a tunneling event.</p>	30

LIST OF ILLUSTRATIONS (Continued)

Figure No.		Page
7-1	Schematic of Schottky barrier transistor fabrication process. (a) LOCOS isolation, (b) gate stack lithography, (c) gate etch and thin oxide spacer formation, and (d) Pt-silicide source drain formation. No implants are used in this process.	35
7-2	Sub-25-nm gate length transistor: (a) Top-down scanning electron micrograph and (b) cross-sectional transmission electron micrograph.	36
7-3	(a) Drain current vs drain voltage and (b) drain current vs gate voltage for low-leakage sub-25-nm pMOS transistor. This device received a single blanket As implant for off-state leakage reduction.	37
7-4	(a) Drain current vs drain voltage and (b) transconductance vs gate voltage for pMOS transistor without implants. Values of cutoff frequency (in GHz) as a function of device bias are plotted in (a) next to the solid circles.	38
7-5	RF test results and extrapolated cutoff frequency f_T values for 22-, 50-, and 70-nm gate length pMOS transistors. The S parameters were measured from 2 to 40 GHz.	39

LIST OF TABLES

Table No.		Page
2-1	Uniformity across Grown Wafer of 50.8 mm Excluding Edge Region of 5 mm	9

INTRODUCTION

1. QUANTUM ELECTRONICS

A cryogenically cooled Yb:YAG laser has been built to demonstrate efficient solid-state laser operation with negligible thermal distortions. Continuous wave power of 120 W in a near diffraction-limited beam has been obtained with 203 W of pump power.

2. ELECTRO-OPTICAL MATERIALS AND DEVICES

A separate-absorber-multiplier avalanche photodiode in the antimonide material system with spectral response at 3.4 μm has been developed that operates in the linear-gain regime. Geiger-mode (above breakdown) operation has been demonstrated in diodes of the multiplier alloy AlGaAsSb.

Exceptional growth uniformity has been demonstrated with a new organometallic vapor-phase epitaxy apparatus, which has a growth tube that differs in several aspects from one used previously. More uniform distribution of reactants delivered across the growth surface is thought to account for improved uniformity.

3. SUBMICROMETER TECHNOLOGY

A new type of material comprising a fluoropolymer blended with silica nanoparticles has been developed to address the need for protective pellicles for 157-nm lithography. This nanocomposite has demonstrated improved longevity when compared with the neat fluoropolymer, despite the fact that the nanoparticle loading increased the initial absorbance of the film.

4. BIOSENSOR AND MOLECULAR TECHNOLOGIES

The sample-preparation cartridge LiNK (Lincoln Nucleic acid Kit) has been successfully tested with the field-deployable RAZOR instrument (Idaho Technology) against Ba spores and Btk spores in growth media, dirty environmental water, and acid-washed sand. The cartridge had been designed for compatibility with the RAZOR instrument.

5. ADVANCED IMAGING TECHNOLOGY

A new charge-coupled device (CCD) architecture for adaptive imaging in ground-based astronomy has been developed. The device is based on the orthogonal-transfer CCD (OTCCD) and consists of a two-dimensional array of small ($\sim 500 \times 500$ pixels) OTCCDs, each of which can be individually addressed and read out independently.

6. ANALOG DEVICE TECHNOLOGY

The use of the superconductive analog to electromagnetically induced transparency (S-EIT) is proposed to demonstrate macroscopic quantum interference in superconductive quantum circuits. S-EIT is shown to measure, with a single pulse of the two S-EIT fields, whether a particular superposition of metastable energy levels (a qubit) has been prepared.

7. ADVANCED SILICON TECHNOLOGY

Results on sub-30-nm gate length pMOSFETs with platinum silicide Schottky-barrier source and drain have demonstrated inherently low series resistance and high drive current, which makes these deeply scaled transistors promising for high-speed analog applications. A sub-25-nm gate length pMOSFET exhibited a cutoff frequency of 280 GHz, the highest reported for a silicon MOS transistor, and off-state leakage current can be easily controlled by augmenting the Schottky barrier height with an optional blanket As implant.

REPORTS ON SOLID STATE RESEARCH

1 MAY THROUGH 31 JULY 2004

PUBLICATIONS

Minimizing Mask Complexity for Advanced Optical Lithography	M. Fritze B. Tyrrell	<i>Proc SPIE</i> 5379 , 30 (2004)
Optically Switched Conductivity of Epitaxial Diamond on Nitrogen Doped Diamond Substrates	M. W. Geis K. E. Krohn J. M. Lawless S. J. Deneault M. F. Marchant J. C. Twichell T. M. Lyszczarz J. E. Butler* D. D. Flechtner* R. Wright*	<i>Appl. Phys. Lett.</i> 84 , 4620 (2004)
Fabrication of Crystalline Organic Waveguides with an Exceptionally Large Electro-optic Coefficient	M. W. Geis R. Sinta W. Mowers S. J. Deneault M. F. Marchant K. E. Krohn S. J. Spector D. R. Calawa T. M. Lyszczarz	<i>Appl. Phys. Lett.</i> 84 , 3729 (2004)
Photoresist Outgassing: A Potential Achilles Heel for Short-Wavelength Optical Lithography?	R. R. Kunz	<i>Proc SPIE</i> 5376 , 1 (2004)
Temperature Dependence of Intermodulation Distortion in YBCO	D. E. Oates S.-H. Park D. Agassi* G. Koren*	<i>Supercond. Sci. Technol.</i> 17 , S290 (2004)

*Author not at Lincoln Laboratory.

Dynamic Response of an Electronically Shuttered CCD Imager	D. D. Rathman D. M. O'Mara M. K. Rose R. M. Osgood III R. K. Reich	<i>IEEE Trans. Electron Devices</i> 51 , 864 (2004)
Effect of Ga-Rich Growth Conditions on the Optical Properties of GaN Films Grown by Plasma-Assisted Molecular Beam Epitaxy	A. V. Sampath* G. A. Garrett* C. J. Collins* P. Boyd* J. Choe* P. G. Newmann* H. Shen* M. Wraback* R. J. Molnar J. M. Caissie*	<i>J. Vac. Sci. Technol. B</i> 22 , 1487 (2004)
Effect of Ca Doping on the Nonlinear Microwave Properties of YBCO Thin Films	D. Seron* D. E. Oates A. C. Anderson G. Hammerl* J. Mannhart* P. J. Hirst* R. G. Humphreys* M. Hein*	<i>Supercond. Sci. Technol.</i> 17 , S422 (2004)
Rapid Cryofixation/Freeze Fracture for the Study of Nanobubbles at Solid-Liquid Interfaces	M. Switkes J. W. Ruberti*	<i>Appl. Phys. Lett.</i> 84 , 4759 (2004)
Microstructure and Optical Properties of Pulsed-Laser-Deposited Iron Oxide Films	T. Tepper* C. A. Ross* G. F. Dionne	<i>IEEE Trans. Magn.</i> 40 , 1685 (2004)
Slab-Coupled Optical Waveguide Lasers: A Review	J. N. Walpole	<i>Proc. SPIE</i> 5365 , 124 (2004)

*Author not at Lincoln Laboratory.

Wafer Bonding and Epitaxial
Transfer of GaSb-Based Epitaxy
to GaAs for Monolithic
Interconnection of
Thermophotovoltaic Devices

C. A. Wang
D. A. Shiau
P. G. Murphy
P. W. O'Brien
R. K. Huang
M. K. Connors
A. C. Anderson
D. Donetsky
S. Anikeev
G. Belenky
D. M. Depoy
G. Nichols

J. Electron. Mater. **33**, 213
(2004)

Self-Organized Vertical
Superlattices in Epitaxial
GaInAsSb

C. A. Wang
C. J. Vineis*
D. R. Calawa

Appl. Phys. Lett. **85**, 594 (2004)

Structure-Property Relationships
in Porous GaN Generated by
Pt-Assisted Electroless Etching
Studied by Raman Spectroscopy

T. L. Williamson*
D. J. Diaz*
P. W. Bohn*
R. J. Molnar

J. Vac. Sci. Technol. B **22**, 925
(2004)

Energy-Scavenging Amplifiers for
Miniature Solid-State Lasers

J. J. Zayhowski
A. L. Wilson, Jr.

Opt. Lett. **29**, 1218 (2004)

PRESENTATIONS[†]

High-Brightness Slab-Coupled
Semiconductor Lasers with Single-
Spatial Large-Diameter Mode

J. P. Donnelly
R. K. Huang
L. J. Missaggia
J. Plant

Conference on Lasers and
Electro-Optics/Quantum
Electronics and Laser Science
Conferences,
San Francisco, California,
16-21 May 2004

*Author not at Lincoln Laboratory.

[†] Titles of presentations are listed for information only. No copies are available for distribution.

Laser Beam Combining:
Techniques and Prospects

T. Y. Fan

Conference on Lasers and
Electro-Optics/Quantum
Electronics and Laser Science
Conferences,
San Francisco, California,
16-21 May 2004

High Power 2.1- μm GaSb-Based
Laser Diode Arrays

R. Huang
M. Manfra
R. Bailey
L. Missaggia

Conference on Lasers and
Electro-Optics/Quantum
Electronics and Laser Science
Conferences,
San Francisco, California,
16-21 May 2004

165-W Cryogenically Cooled
Yb:YAG Laser

D. J. Ripin
J. R. Ochoa
R. L. Aggarwal
T. Y. Fan

Conference on Lasers and
Electro-Optics/Quantum
Electronics and Laser Science
Conferences,
San Francisco, California,
16-21 May 2004

Two Decades of Photonic Analog-
to-Digital Converters

R. C. Williamson

Conference on Lasers and
Electro-Optics/Quantum
Electronics and Laser Science
Conferences,
San Francisco, California,
16-21 May 2004

Simultaneous Optimization of the
Nonlinear Microwave Response of
YBaCuO Films and MgO
Substrates

M. Hein*
P. J. Hirst*
R. G. Humphreys*
S-H. Park
D. E. Oates
D. Seron*
J. Derov*

8th Symposium on High-
Temperature Superconductors
in High-Frequency Fields,
Begur, Spain,
26-29 May 2004

*Author not at Lincoln Laboratory.

Temperature Dependence of
Intermodulation Distortion in
YBCO Nonlinearity at the Intrinsic
Limit

D. Oates
S-H. Park
D. Agassi*

8th Symposium on High-
Temperature Superconductors
in High-Frequency Fields,
Begur, Spain,
26-29 May 2004

Comparison of YBCO and
Ca-Substituted YBCO Thin Films
for Microwave Applications

D. Seron*
D. E. Oates
A. C. Anderson
J. Halbritter*
J. Mannhart*
G. Hammerl*
M. A. Hein*
P. J. Hirst*
R. G. Humphreys*

8th Symposium on High-
Temperature Superconductors
in High-Frequency Fields,
Begur, Spain,
26-29 May 2004

Effects of Radiative Recombination
and Photon Recycling on Minority
Carrier Lifetime in Epitaxial
GaInAsSb Lattice-Matched to GaSb

S. Anikeev*
G. Ning*
D. Donetsky*
G. Belenky*
S. Luryi*
C. A. Wang
D. A. Shiau
M. Dashiell*
J. Beausang*
G. Nichols*

12th International Conference
on Metal Organic Vapor Phase
Epitaxy,
Lahaina, Hawaii,
30 May–4 June 2004

Progress and Continuing
Challenges in GaSb-Based III-V
Alloys and Heterostructures Grown
by Organometallic Vapor Phase
Epitaxy

C. A. Wang

12th International Conference
on Metal Organic Vapor Phase
Epitaxy,
Lahaina, Hawaii,
30 May–4 June 2004

*Author not at Lincoln Laboratory.

Liquid Immersion Optical
Lithography—Why, How, and
When?

M. Rothschild
T. M. Bloomstein
R. R. Kunz
V. Liberman
M. Switkes
S. T. Palmacci
J. H. C. Sedlacek
D. E. Hardy
A. Grenville*

Electron, Ion, Photon Beam
Technology and
Nanofabrication Conference,
San Diego, California,
1-4 June 2004

Bubbles in Immersion Lithography

M. Switkes
M. Rothschild
T. A. Shedd*
H. Burnett*
J. W. Ruberti*

Electron, Ion, Photon Beam
Technology and
Nanofabrication Conference,
San Diego, California,
1-4 June 2004

Optical Sampling for High-Speed,
High-Resolution Analog-to-Digital
Conversion

P. W. Juodawlkis
J. J. Hargreaves
R. D. Younger
R. C. Williamson
G. E. Betts
J. C. Twichell

IEEE International Microwave
Symposium,
Fort Worth, Texas,
6-11 June 2004

Large Tuning Range Analog and
Multi-bit MEMS Varactors

J. Muldavin
C. Bozler
S. Rabe
C. Keast

IEEE International Microwave
Symposium,
Fort Worth, Texas,
6-11 June 2004

Reliability Testing and
Enhancement of RF MEMS
Capacitive Switches

J. B. Muldavin
C. O. Bozler
J. Vian
S. Targonski
C. L. Keast
M. A. Gouker

IEEE International Microwave
Symposium,
Fort Worth, Texas,
6-11 June 2004

*Author not at Lincoln Laboratory.

Wavelength Tuning of Aluminum-Free, Mid-IR Semiconductor Lasers

A. K. Goyal
G. W. Turner
A. Sanchez
M. F. Manfra
P. J. Foti
P. O'Brien

16th Solid State and Diode Laser Technology Review, Albuquerque, New Mexico, 8-10 June 2004

915-nm AlGaAs-InGaAs Slab-Coupled Optical Waveguide Lasers and Arrays for Wavelength Beam Combining

R. Huang
J. Donnelly
L. Missaggia
C. Harris

16th Solid State and Diode Laser Technology Review, Albuquerque, New Mexico, 8-10 June 2004

Room Temperature 2- μ m Diode Laser Arrays

R. Huang
M. Manfra
R. Bailey
L. Missaggia

16th Solid State and Diode Laser Technology Review, Albuquerque, New Mexico, 8-10 June 2004

165-W Cryogenically Cooled Yb:YAG Laser

D. J. Ripin
J. R. Ochoa
R. L. Aggarwal
T. Y. Fan

16th Solid State and Diode Laser Technology Review, Albuquerque, New Mexico, 8-10 June 2004

Automated CANARY Testbed for Fast Bioaerosol Identification

J. D. Harper

Federal Bio-Chem Detection R&D Opportunities—Detection Technology Summit, Washington, D. C., 9-11 June 2004

UV Luminescence Spectroscopy and Discrimination of Bioaerosols

T. H. Jeys
D. J. Ripin

Federal Bio-Chem Detection R&D Opportunities—Detection Technology Summit, Washington, D. C., 9-11 June 2004

Analysis of Recombination
Processes in 0.5–0.6 eV Epitaxial
GaInAsSb Lattice-Matched to GaSb

D. Donetsky*
S. Anikeev*
G. Ning*
G. Belenky*
S. Luryi*
C. A. Wang
D. A. Shiau
M. Dashiell*
J. Beausang*
G. Nichols*

6th International Conference on
the Thermophotovoltaic
Generation of Electricity,
Freiburg, Germany,
14-16 June 2004

Hybrid Back Surface Reflector
GaInAsSb Thermophotovoltaic
Devices

R. Huang
C. Wang
M. Connors
G. Turner
M. Dashiell*

6th International Conference on
the Thermophotovoltaic
Generation of Electricity,
Freiburg, Germany,
14-16 June 2004

Antimony-Based III-V
Thermophotovoltaic Materials and
Devices

C. A. Wang

6th International Conference on
the Thermophotovoltaic
Generation of Electricity,
Freiburg, Germany,
14-16 June 2004

Wafer-Bonding and Epitaxial
Transfer of GaInAsSb/GaSb to
GaAs Substrates for Monolithic
Series Interconnection of
Thermophotovoltaic Cells

C. A. Wang
R. K. Huang
D. A. Shiau
P. G. Murphy
P. W. O'Brien
A. C. Anderson
D. Donetsky*
S. Anikeev*
G. Belenky*
S. Luryi*
G. Nichols*

6th International Conference on
the Thermophotovoltaic
Generation of Electricity,
Freiburg, Germany,
14-16 June 2004

*Author not at Lincoln Laboratory.

Devices and Protocols for the
Recovery of Organisms and Nucleic
Acids from Complex Samples

L. Parameswaran

5th BioDetection Technologies:
Technological Responses to
Biological Threats,
Washington, D. C.,
18 June 2004

Progress in X-Ray CCD Sensor
Performance for the Astro-E2
X-Ray Imaging Spectrometer

M. W. Bautz*
S. E. Kissel*
G. Y. Prigozhin*
B. LaMarr*
B. Burke
J. A. Gregory

SPIE Astronomical Telescopes
and Instrumentation,
Glasgow, Scotland,
21-25 June 2004

The Orthogonal-Transfer Array:
A New CCD Architecture for
Astronomy

B. Burke
J. Tonry*
M. Cooper
G. Luppino*
G. Jacoby*
R. Bredthauer*
K. Boggs*
M. Lesser*
P. Onaka*
D. Young
P. Doherty*
D. Craig*

SPIE Astronomical Telescopes
and Instrumentation,
Glasgow, Scotland,
21-25 June 2004

A Novel CCD Design for Curvature
Wavefront Sensing

R. J. Dorn*
J. E. Beletic*
B. E. Burke

SPIE Astronomical Telescopes
and Instrumentation,
Glasgow, Scotland,
21-25 June 2004

X-Ray CCD with Charge Injection
Structure

G. Prigozhin*
B. Burke
M. Bautz*
S. Kissel*
B. LaMarr*
M. Freytsis*

SPIE Astronomical Telescopes
and Instrumentation,
Glasgow, Scotland,
21-25 June 2004

*Author not at Lincoln Laboratory.

LLiST—A New Star Tracker
Camera for Tip-Tilt Correction at
IOTA

P. A. Schuller*
M. G. Lacasse*
D. Lydon*
E. Pedretti*
F. P. Schloerb*
W. A. Traub*
W. M. McGonagle
R. K. Reich

SPIE Astronomical Telescopes
and Instrumentation,
Glasgow, Scotland,
21-25 June 2004

Measurements of Recombination
Rates in Low-Doped Epitaxial
GaInAsSb Lattice-Matched to GaSb
by Frequency Response of
Photoluminescence

D. Donetsky*
S. Anikeev*
N. Gu*
G. Belenky*
S. Luryi*
C. A. Wang
D. A. Shiau
M. Dashiell*
J. Beausang*
G. Nichols*

46th Electronic Materials
Conference,
Notre Dame, Indiana,
23-25 June 2004

Static and Dynamic Measurements
of Recombination Lifetime in
Narrow-Gap GaInAsSb Lattice-
Matched to GaSb

S. Anikeev*
D. Donetsky*
G. Belenky*
S. Luryi*
C. A. Wang
D. A. Shiau
M. Dashiell*
J. Beausang*
G. Nichols*

6th International Conference on
Mid-Infrared Optoelectronics
Materials and Devices,
St. Petersburg, Russia,
28 June–1 July 2004

Crystalline Waveguides with
Exceptionally Large Electro-optic
Coefficients

M. W. Geis
S. J. Spector
T. M. Lyszczarz

OSA Topical Meeting on
Integrated Photonics Research,
San Francisco, California,
30 June–2 July 2004

*Author not at Lincoln Laboratory.

Submicrosecond, Submilliwatt,
Silicon on Insulator Thermo-optic
Switch

M. W. Geis
S. J. Spector
R. C. Williamson
T. M. Lyszczarz

OSA Topical Meeting on
Integrated Photonics Research,
San Francisco, California,
30 June–2 July 2004

Hybrid Multi-mode/Single-mode
Waveguides for Low Loss

S. J. Spector
M. W. Geis
D. M. Lennon
R. C. Williamson
T. M. Lyszczarz

OSA Topical Meeting on
Integrated Photonics Research,
San Francisco, California,
30 June–2 July 2004

ORGANIZATION

SOLID STATE DIVISION

D. C. Shaver, Head
R. W. Ralston, Associate Head
N. L. DeMeo, Jr., Assistant
Z. J. Lemnios, Senior Staff
K. J. Challberg, Administrative Staff
L. K. Pacheco, Administrative Staff
J. D. Pendergast, Administrative Staff

SUBMICROMETER TECHNOLOGY

M. Rothschild, Leader
T. M. Lyszczarz, Assistant Leader
T. H. Fedynyshyn, Senior Staff
R. R. Kunz, Senior Staff

Astolfi, D. K.
Bloomstein, T. M.
Cann, S. G.
Efremow, N. N., Jr.
Geis, M. W.
Goodman, R. B.
Krohn, K. E.
Leibowitz, F. L.
Lennon, D. M.

Lieberman, V.
Palmacci, S. T.
Pottebaum, I. S.
Sedlacek, J. H. C.
Spector, S. J.
Switkes, M.
Wynn, C. M.
Yoon, J. U.

QUANTUM ELECTRONICS

A. Sanchez-Rubio, Leader
T. Y. Fan, Assistant Leader
T. H. Jeys, Senior Staff
J. J. Zayhowski, Senior Staff

Aggarwal, R. L.
Augst, S. J.
Chann, B.
Daneu, J. L.
DiNatale, W. F.
Goyal, A. K.
Herzog, W. D.
Hybl, J. D.

Le, X. T.
Lynch, E. J.
O'Brien, P. W.
Ochoa, J. R.
Ranka, J. K.
Ripin, D. J.
Tysk, S. M.

ELECTRO-OPTICAL MATERIALS AND DEVICES

J. C. Twichell, Leader
G. W. Turner, Assistant Leader
J. P. Donnelly, Senior Staff
D. L. Spears, Senior Staff
C. A. Wang, Senior Staff
R. C. Williamson, Senior Staff

Bailey, R. J.
Calawa, D. R.
Calawa, S. D.
Connors, M. K.
Duerr, E. K.
Goodhue, W. D.
Groves, S. H.
Hargreaves, J. J.
Harman, T. C.
Harris, C. T.
Huang, R. K.

Juodawlkis, P. W.
LaForge, B. E.
Liau, Z. L.
Mahan, J. M.
Mahoney, L. J.
Manfra, M. J.
McIntosh, K. A.
McNulty, D. D.
Missaggia, L. J.
Molnar, R. J.

Mull, D. E.
Napoleone, A.
Nitishin, P. M.
Oakley, D. C.
O'Donnell, F. J.
Plant, J. J.
Shiau, D. A.
Swint, R. B.
Verghese, S.
Younger, R. D.

BIOSENSOR AND MOLECULAR
TECHNOLOGIES

M. A. Hollis, Leader
T. H. Rider, Senior Staff

Bohane, M. D.	Parameswaran, L.
Cabrera, C. R.	Petrovick, M. S.
Graves, C. A.	Riley, M. M.
Harper, J. D.	Schmidt, T. L.
Hogan, K. E.	Schwoebel, E. D.
Lacirignola, J. J.	Theriault, K. A.
Mathews, R. H.	Towle, T. A.
Nargi, F. E.	Wick, S. T.
Pancoast, J. S.	Zook, C. E.

ANALOG DEVICE TECHNOLOGY

M. A. Gouker, Leader
L. M. Johnson, Assistant Leader

Aversa, J. C.	Murphy, P. G.
Bolkhovsky, V.	Oates, D. E.
Drangmeister, R. G.	Oliver, W. D.
Fitch, G. L.	Sage, J. P.
Ieni, S.	Santiago, D. D.
Lyons, W. G.	Slattery, R. L.
Macedo, E. M., Jr.	Straayer, M. Z.
Messier, A. V.	Weir, T. J.

ADVANCED IMAGING TECHNOLOGY

R. K. Reich, Leader
B. B. Kosicki, Associate Leader
J. A. Gregory, Assistant Leader
B. E. Burke, Senior Staff

Aull, B. F.	Loomis, A. H.
Ciampi, J. S.	McGonagle, W. H.
Cooper, M. J.	O'Mara, D. M.
Craig, D. M.	Osgood, R. M.
Daniels, P. J.	Percival, K. A.
Doherty, C. L., Jr.	Rathman, D. D.
Doherty, P. E.	Renzi, M. J.
Dolat, V. S.	Rose, M. K.
Felton, B. J.	Ruth, W. M.
Johnson, K. F.	Stern, A.
Lambert, R. D.	Stevenson, C. N.
Lind, T. A.	Young, D. J.

ADVANCED SILICON TECHNOLOGY

C. L. Keast, Leader
V. Suntharalingam, Assistant Leader
P. W. Wyatt, Senior Staff

Austin, E. E.	Hu, W.
Berger, R.	Knecht, J. M.
Bozler, C. O.	Muldavin, J. B.
Brunelle, M. R.	Newcomb, K. L.
Burns, J. A.	Rabe, S.
Chen, C. K.	Soares, A. M.
Chen, C. L.	Tyrrell, B. M.
D'Onofrio, R. P.	Warner, K.
Fritze, M.	Wheeler, B. D.
Gouker, P. M.	Wlodarczak, T. J.
Healey, P. D.	Yost, D.-R.
Healey, R. E.	Young, G. R.

1. QUANTUM ELECTRONICS

1.1 120-W CRYOGENICALLY COOLED Yb:YAG LASER

Power scaling in solid state lasers is generally limited by thermo-optical distortions, thermally induced birefringence, or stress fracture. Solid state laser efficiency, meanwhile, depends on spectroscopic properties (quantum defect and saturation intensity) of the gain medium as well as the pumping geometry. Cryogenically cooled (~ 100 K) Yb:YAG has potential for efficient high-power solid state lasers with good spatial beam quality because of the material's comparatively good thermal and optical properties at low temperatures [1],[2]. At 100 K, YAG has a significantly higher thermal conductivity, lower thermo-optic coefficient, and lower coefficient of thermal expansion than at room temperature. Each of these properties results in reduced thermo-optic effects at low temperature. Furthermore, Yb:YAG has spectroscopic properties at cryogenic temperatures that favor high laser efficiency. For example, at 100 K Yb:YAG energy levels become four-level, the saturation intensity decreases, the quantum defect is only 9%, and an absorption band at 940 nm remains broad enough for diode pumping.

To estimate the magnitude of thermo-optic effects at cryogenic temperatures, the thermal conductivity κ , thermo-optic coefficient dn/dT , and coefficient of thermal expansion α of YAG were measured as a function of temperature from 100 to 300 K, as shown in Figure 1-1. At 100 K, undoped YAG was measured to have κ of $46 \text{ W/m} \cdot \text{K}$, dn/dT at $1.064 \mu\text{m}$ of $0.44 \times 10^{-6} \text{ K}^{-1}$, and α of $2.2 \times 10^{-6} \text{ K}^{-1}$. It is possible to estimate the relative magnitude of the thermal load for which thermo-optic distortions

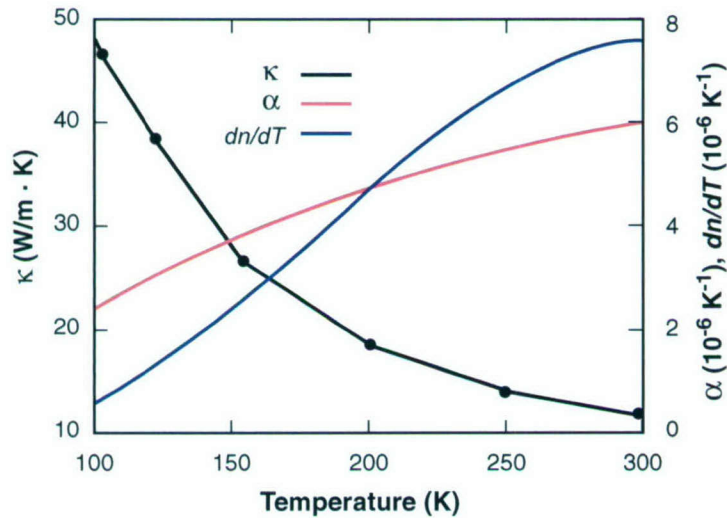


Figure 1-1. Thermal conductivity κ , coefficient of thermal expansion α , and thermo-optic coefficient dn/dT of YAG measured from 100 K to room temperature.

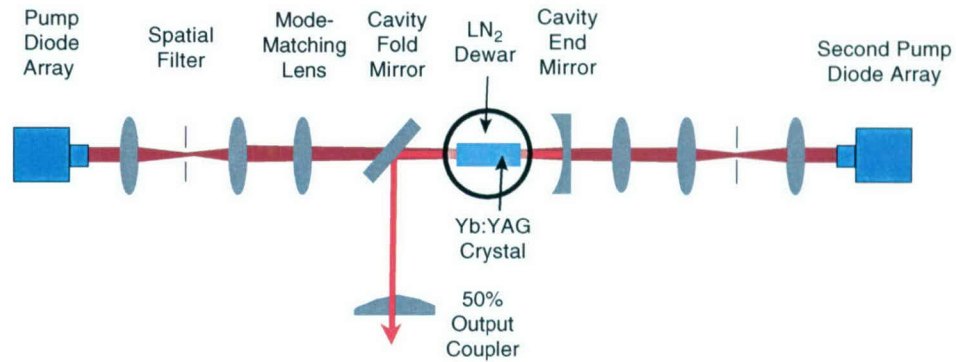


Figure 1-2. Schematic of diode end-pumped cryogenically cooled Yb:YAG laser.

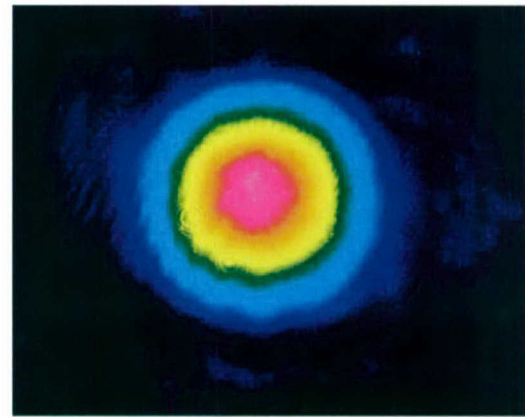
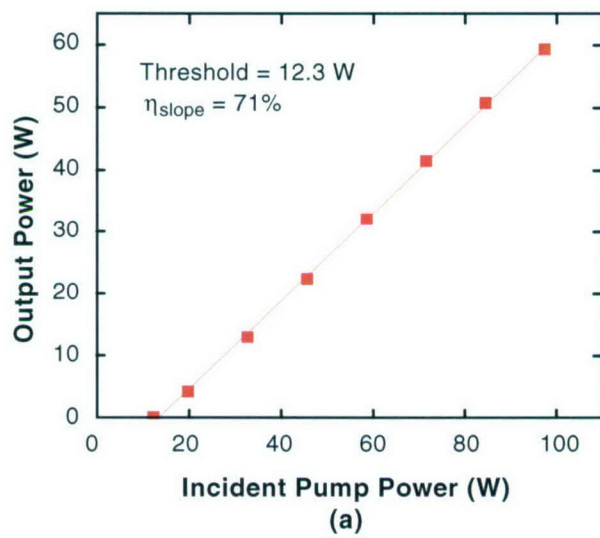


Figure 1-3. (a) Output power of cryogenically cooled Yb:YAG laser as a function of incident diode pump power, and (b) beam profile at 60-W output power.

and thermally induced birefringence become significant using figures of merit defined as $FOM_{OPD} = \kappa/(dn/dT)$ and $FOM_B = \kappa/\alpha$, respectively. The ratios of the 100-K and room-temperature figures of merit for constant heat loading are 74 for thermo-optic distortion and 12 for thermally induced birefringence.

A diode-pumped Yb:YAG laser oscillator was built to demonstrate the utility of cryogenically cooling. A schematic of the laser oscillator is shown in Figure 1-2. A composite 5-at.% Yb:YAG crystal is indium soldered into a copper heat sink and mounted in a liquid nitrogen cryostat. The crystal is double end-pumped by two high-radiance free-space diode laser modules (Apollo Instruments) operating at 940 nm. Up to 97 W of pump power from one pump module and 106 W from the second pump module are incident upon the laser crystal after transmission through coupling optics and a side-lobe-removing spatial filter. The laser cavity is a simple concave-convex resonator with a single intracavity fold mirror, two antireflection-coated dewar windows, and a 50% output coupler.

The end-pumped oscillator was first optimized using a single pump module. Continuous wave output power up to 60 W with a pump power of 97 W was generated, as shown in Figure 1-3(a). The pump threshold was 12.3 W and the slope efficiency 71%. The beam profile measured under these conditions, shown in Figure 1-3(b), closely approximated a Gaussian mode. By using a knife edge technique, this beam was measured to be near diffraction limited with an M^2 of 1.2. In addition to the good beam quality measured with the single pump module laser, negligible thermal lensing and thermal birefringence were observed. After adding the second pump module through the end mirror, cw output power of 120 W with qualitatively good beam quality was obtained.

D. J. Ripin
J. Ochoa

R. L. Aggarwal
T. Y. Fan

REFERENCES

1. P. Lacovara, H. K. Choi, C. A. Wang, R. L. Aggarwal, and T. Y. Fan, *Opt. Lett.* **16**, 1089 (1991).
2. T. Y. Fan, T. Crow, and B. Hoden, *Proc. SPIE* **3381**, 200 (1998).

2. ELECTRO-OPTICAL MATERIALS AND DEVICES

2.1 ANTIMONIDE-BASED AVALANCHE PHOTODIODES FOR THE MID-IR

Avalanche photodiodes (APDs) operating in the Geiger mode (above breakdown) for single-photon detection have been developed at Lincoln Laboratory using silicon for detecting visible radiation [1], gallium nitride for detecting ultraviolet radiation [2], and III-V compounds lattice matched to InP for detecting near-infrared (NIR) radiation [3]. These APDs enable systems such as laser ranging and high-bandwidth communications. In certain scenarios, an APD capable of detecting longer-wavelength photons is desirable. To access wavelengths beyond the NIR using a direct-bandgap semiconductor requires the antimonide material system. Lattice-matched alloys grown on GaSb can absorb radiation to 4 μm .

High-speed or high-sensitivity APDs often rely on a separate-absorber-multiplier (SAM) design that allows independent optimization of both the material and electric field in the absorber and multiplier layers. For long-wavelength Geiger-mode APDs, this separation is important because the material required for absorbing the wavelength of interest frequently has a small enough bandgap that it is not able to stand off the electric field required for Geiger-mode operation. By incorporating a thin, doped field stop layer between the absorber and multiplier, the electric field in each layer can be tuned. For optimum Geiger-mode operation, the total doping in the field stop should be such that the absorber layer fully depletes just as the field in the multiplier becomes high enough to initiate breakdown.

Using these principles, we designed a nominal SAM APD structure in the Sb material system. Three materials are required for the nominal APD design: InAsSb for the mid-wave-infrared absorbing region, AlGaAsSb for the field stop and avalanche regions, and GaSb for the cap and contact layers. (The multiplication layer quaternary is denoted by the aluminum fraction; the remaining element fractions are chosen for lattice match to the GaSb substrate.) InAsSb is the smallest-bandgap alloy lattice matched with GaSb with absorption to 4 μm . The first-generation devices used 90% AlGaAsSb because of the large bandgap and the slightly lower susceptibility to oxidation when compared to 100% AlAsSb. Subsequent work indicates, however, that material quality issues dictate a lower aluminum fraction.

The APDs were grown using molecular beam epitaxy (MBE). Required conditions for lattice-matched growth as well as controllable doping of all layers were achieved through numerous test growths. In order of growth, the first-generation SAM APD device layers consisted of a 1.0- μm -thick p^+ GaSb buffer layer, a 1.0- μm -thick p^+ 90% AlGaAsSb layer, a 1.0- μm -thick unintentionally doped 90% AlGaAsSb multiplier layer, a 90-nm-thick n 90% AlGaAsSb field stop layer, a 1.0- μm -thick unintentionally doped InAsSb absorber layer, and a 1.0- μm -thick p -GaSb contact layer. The type-II band alignment of InAsSb to GaSb requires that the cathode contact be p doped rather than n doped as normally expected, so that the electrons can exit the absorber. An x-ray diffraction rocking curve showed excellent lattice match for all layers.

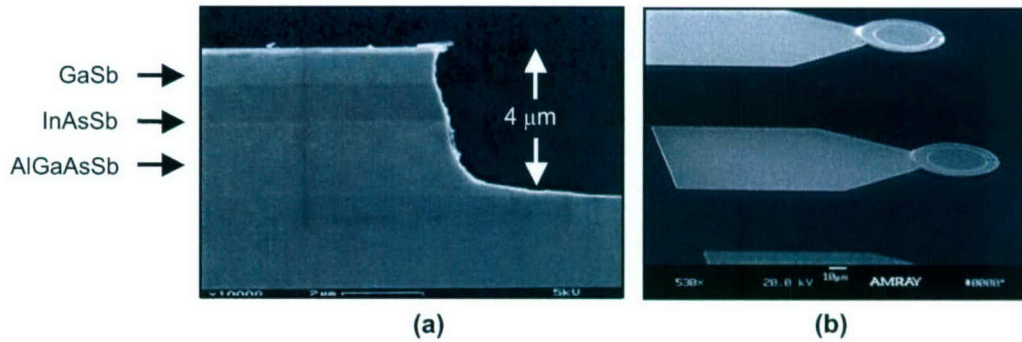


Figure 2-1. Scanning electron micrographs of (a) etched device mesa, and (b) passivated 30- μm -diameter devices with annular contacts and bond pads.

Devices were defined by etching at least 4 μm into the epitaxial layers, using either wet chemical or dry etching. The results presented are from devices wet etched with a mixture of 3% bromine and ethylene glycol. Figure 2-1(a) shows the cross section of an etched APD. Figure 2-1(b) shows the top view of two 30- μm devices with annulus contact for top-side optical access and a large metal pad for probe or wire bond contact.

Testing the APDs involved illuminating the device with the wavelength of interest while applying a reverse bias. The optical source was a HeNe laser operating at 3.39 μm . The laser output was chopped, and the resulting modulated current through the APD was detected in a lock-in amplifier. Ideally, optically excited carriers are swept out of the absorbing region into the multiplication region where they undergo multiplication. Capacitance-voltage profiling indicated, however, that the first-generation APDs entered breakdown before the field stop layer fully depleted; therefore, the only optically excited carriers entering the multiplication region were those that diffused out of the absorber. This reliance on diffusion explains the low quantum efficiency (approximately 10^{-5}) and need to use lock-in detection of the photoinduced signal. A thinner field stop layer would alleviate this problem. A representative reverse bias current-voltage curve is shown in Figure 2-2 along with the arbitrarily scaled lock-in signal. The lock-in measurement does not extend to lower voltages because the signal was in the noise. The rapid increase of the lock-in output with the rapid increase in dc current is strong evidence of multiplication of photogenerated carriers. To our knowledge, this is the first-ever observation of avalanche gain in a $\lambda > 2.3\text{-}\mu\text{m}$ SAM APD based on the Sb material system.

Geiger-mode operation of these devices was not observed. Geiger-mode breakdown in this material system was measured, however, in homojunction PIN diodes composed of multiplier alloy. At room temperature and 77 K, multiplier-only diodes gate biased above breakdown for a brief ($\sim 1\text{ }\mu\text{s}$) time demonstrate characteristic current pulses that occur at random instants after the beginning of the gate. Figure 2-3 shows the rate of these breakdown events in the dark for a PIN diode consisting of 1 μm of

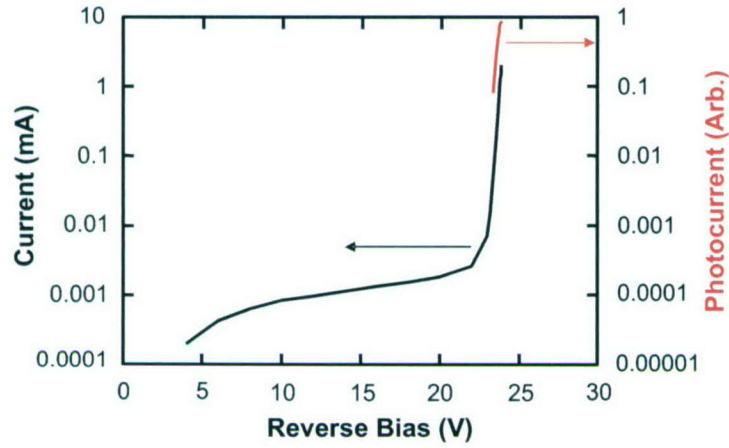


Figure 2-2. Current vs voltage characteristic of 30- μm -diameter separate-absorber-multiplier avalanche photodiode operated at 77 K. The photocurrent vs voltage characteristic was measured simultaneously while illuminating the device with a chopped 3.39- μm optical source.

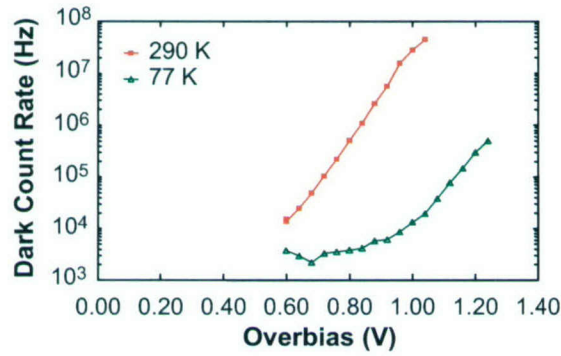


Figure 2-3. Dark count rate vs overbias for a 41% AlGaAsSb PIN diode operating in the Geiger mode. The breakdown voltage at 290 K is 29.91 V and at 77 K is 26.62 V.

unintentionally doped 41% AlGaAsSb between a p and an n layer of the same material. Photon detection efficiency has not been measured on these diodes, but the rapid increase in the dark count rate with overbias is likely due to an increase in band-to-band tunneling. This phenomenon is not desirable, and material improvements may be required to reduce this source of dark carriers. Second-generation SAM APD devices will incorporate this 41% AlGaAsSb alloy.

We have achieved two major milestones in the development of mid-infrared APDs for Geiger-mode operation. We observed photoresponse at 3.39 μm and avalanche multiplication of photoexcited carriers in

devices from the first generation of SAM APDs. We also demonstrated Geiger-mode breakdown events in multiplier layers lattice matched to the absorber.

E. K. Duerr	M. J. Manfra	J. P. Donnelly
G. W. Turner	D. B. Hoyt	L. J. Mahoney
K. M. Molvar	K. A. McIntosh	J. K. Ranka

2.2 OMVPE GROWTH OF InGaAsP/InP

A close-coupled showerhead (CCS) organometallic vapor-phase epitaxy (OMVPE) reactor, developed by the Thomas Swan Co., Ltd., has replaced an older reactor for growth of $\text{In}_{1-x}\text{Ga}_x\text{As}_y\text{P}_{1-y}$ alloys. The older reactor, developed at Lincoln Laboratory, had single-wafer capability and operated at atmospheric pressure in a chimney geometry (upward flow). A sidearm attached to the chimney permitted susceptor rotation. The new reactor has multiwafer capability (e.g., six 50.8-mm-diameter wafers). A showerhead (matrix of many small holes), about 11 mm above a rotating susceptor, permits uniform injection of reactants over the growth surfaces. It has been operated at a pressure of 100 torr. Trimethylindium (TMI), trimethylgallium (TMG), arsine (AsH_3), and phosphine (PH_3) have been used as the source materials for both reactors.

In the old growth tube, reactants and H_2 carrier gas were injected and allowed to develop into a uniform flow pattern before flowing across the substrate. Without rotation, this gave a leading-to-trailing edge growth rate variation of 20% or more. Susceptor rotation reduced this variation by about 10 times, but the growth rate at the center was at least 2% less than the maximum, which occurred about 20 mm from the center [4]. Furthermore, for growth of InGaAs, with the center lattice matched to the InP substrate, the 20-mm-radius region was in tension (Ga rich) by about 200 arc sec ($a/a_0 = 8 \times 10^{-4}$, where a_0 is the InP lattice parameter).

For the CCS reactor, there is no measurable variation in InP growth rate across 40 mm of a 50.8-mm wafer to within the <1% accuracy to which it can be measured by x-ray techniques. Also, for InGaAs growth, the lattice constant variation in the CCS reactor is 10 times less than in the old reactor, and this is mirrored in the very small (<1 nm) variation in the photoluminescence (PL) wavelength over the wafer. Data for the old and new reactor are summarized in Table 2-1.

To some degree, the In-Ga incorporation ratio is temperature dependent. In both old and new reactors, good temperature uniformity has been demonstrated by growth of $\text{In}_{1-x}\text{Ga}_x\text{As}_y\text{P}_{1-y}$ with highly uniform composition. Therefore, variations in InGaAs growth are thought to be due to nonuniformity in the flow of source material across the wafer. Temperature uniformity is much more important for InGaAsP alloy growth, with AsH_3 and PH_3 as sources, primarily because of the incomplete pyrolysis of PH_3 at the 650°C growth temperature. Although good uniformity of InGaAsP in the new reactor has been measured, it has yet to be optimized by making small adjustments to the temperature profile.

TABLE 2-1

Uniformity across Grown Wafer of 50.8 mm Excluding Edge Region of 5 mm

	Chimney Reactor	CCS Reactor
Thickness variation	2%	<1%
Stacked for InGaAs/InP	200 arc sec	25 arc sec
PL wavelength variation for InGaAs	>6 nm	<1 nm

A related factor in InGaAsP growth is the ability to grow alloys of small As content, where the reproducibility and insensitivity to factors such as growth rate depend strongly on the PH_3 pyrolysis (and consequent metering of small flows of AsH_3). For the old reactor, alloys with $y < 0.2$ were difficult to grow with reasonable flows, whereas those with $y < 0.08$ have been readily grown in our CCS reactor. Curves summarizing the data from each reactor are shown in Figure 2-4. Changes in operating pressure have been found to strongly affect dopant incorporation but not other factors for $\text{In}_{1-x}\text{Ga}_x\text{As}_y\text{P}_{1-y}$ alloy growth [5]. Consequently, improved behavior for low-As alloys in the CCS reactor is more likely attributable to longer residence time than to differences in operating pressure.

In summary, a new CCS reactor, which has replaced our chimney reactor, has provided significant improvements in OMVPE growth of InGaAsP alloys. Even flow of reactants over the growth surface, resulting from the showerhead injector geometry, is thought to account for the exceptional uniformity of

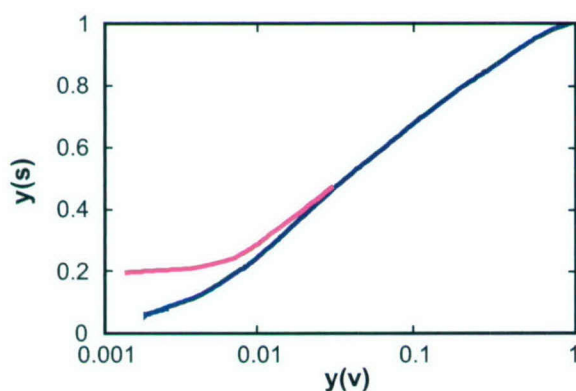


Figure 2-4. Curves summarizing the group V vapor-solid data, with $y(v)$ the As fraction in the vapor and $y(s)$ that in the solid. The lower curve fits the close-coupled showerhead (CCS) reactor data well, and the upper curve represents the lower limit of scattered data for the chimney reactor. The comparison shows the greater accessibility to low $y(s)$ values in the CCS reactor.

growth thickness and composition across the grown wafer. More complete pyrolysis of PH_3 in the CCS reactor facilitates growth of alloys of very low As content.

D. Oakley	A. Napoleone
S. Groves	S. Vernon

REFERENCES

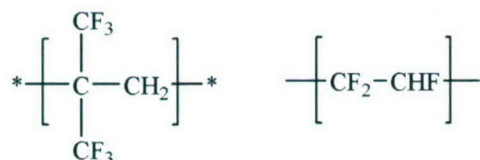
1. B. F. Aull, A. H. Loomis, D. J. Young, R. M. Heinrichs, B. J. Felton, P. J. Daniels, and D. J. Landers, *Lincoln Lab. J.* **13**, 335 (2002).
2. S. Verghese, K. A. McIntosh, R. J. Molnar, L. J. Mahoney, R. L. Aggarwal, M. W. Geis, K. M. Molvar, E. K. Duerr, and I. Melngailis, *IEEE Trans. Electron Devices* **48**, 502 (2001).
3. K. A. McIntosh, J. P. Donnelly, D. C. Oakley, A. Napoleone, S. D. Calawa, L. J. Mahoney, K. M. Molvar, E. K. Duerr, S. H. Groves, and D. C. Shaver, *Appl. Phys. Lett.* **81**, 2505 (2002).
4. S. C. Palmateer, S. H. Groves, J. W. Caunt, and D. L. Hovey, *J. Electron. Mater.* **18**, 645 (1989).
5. A. Ougazzaden, J. D. Ganiere, Y. Gao, E. V. K. Roa, B. Sermage, C. Kazmierski, and A. Mircea, *J. Cryst. Growth* **107**, 761 (1991).

3. SUBMICROMETER TECHNOLOGY

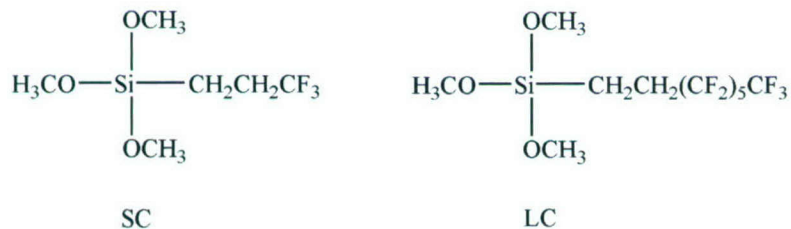
3.1 NANOCOMPOSITE APPROACHES TOWARD PELLICLES FOR 157-nm LITHOGRAPHY

Soft pellicles have been identified as a key hurdle in the implementation of 157-nm lithography. New fluoropolymers, based on unique combinations of perfluorinated and semifluorinated monomers, have been developed for this application [1]. Although high transmission has been demonstrated, all candidate materials to date show rapid degradation in transmission, within a few J/cm² total dose. The radiation-induced transmission failure is probably caused by photogenerated radicals, which upon rearrangement form absorptive unsaturated bonds. One possible way to control the photochemical darkening is, therefore, to introduce radical scavengers in the thin film. Alternatively, radical formation can be reduced by decreasing the number of photocleavable sites on the film. Here, we report on our attempts to follow both paths by incorporating a large fraction of inorganic transparent nanoparticles in the film. Such particles, which are ~10 nm in diameter, and chemically are mainly SiO₂, would at least replace the polymers, thus diluting the number of photoactive molecules. In addition, the surfaces may provide quenching sites of reactive photogenerated radicals.

Since the as-received particles were difficult to disperse in the fluoropolymer, we also prepared nanoparticles with surface termination that included fluorinated moieties. As will be shown below, the surface terminations had little effect on film forming or film optical properties. The fluoropolymer, provided by DuPont and designated as 2P, is a copolymer with the structure



The silica nanoparticles (ST-S), obtained from Nissan Chemical, had a nominal size of 8–10 nm and were supplied as a 30% solution in isopropanol. Surface modifying agents 3,3,3-trifluoropropyl trimethoxysilane (designated as SC, short chain) and tridecafluoro-1,1,2,2-tetrahydrooctyl trimethoxysilane (LC, long chain) were obtained from Gelest; SC and LC chemical structures are



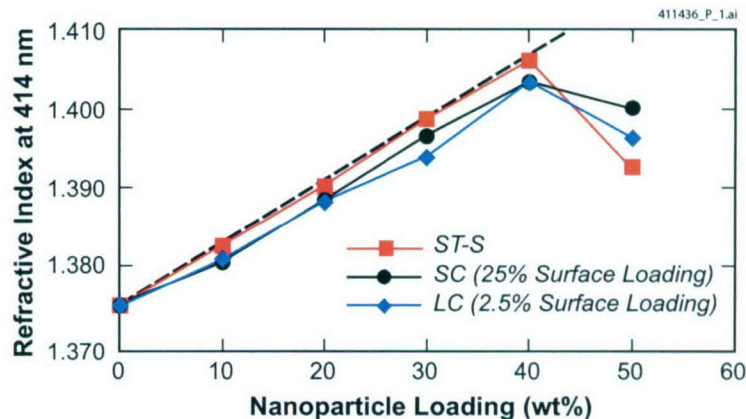


Figure 3-1. Refractive index at 414 nm as a function of nanoparticle loading. Three curves are shown: bare nanoparticles (ST-S) as well as two surface modifications: short chain (SC) at 25% surface loading and long chain (LC) at 2.5% surface loading. Also, a linear fit to the ST-S data is shown (dashed line), based on a prediction from effective medium approximation, as described in the text.

Films of 2P polymer 1 μm thick with varying nanoparticle loadings were spun cast onto CaF_2 substrates. Three surface terminations of nanoparticles were employed: bare (ST-S) particles, SC at 25% surface loading, and LC at 2.5% surface loading. The films were clear and uniform up to $\sim 40\text{-wt}\%$ loading, above which they appeared hazy.

The refractive index of the films was determined at 414 nm with a Metricon prism coupler, with results shown in Figure 3-1. In this figure, all the curves exhibit a linear increase in index with nanoparticle loading up to 40 wt%, at which point the linear trend breaks. The linear part of the refractive index curve may be fit with an effective media approximation, assuming a refractive index of 1.435 for the nanoparticles (compared to $n = 1.47$ for bulk fused silica). The break above 40 wt%, along with the visual appearance of the films, suggests that, up to 40-wt% loading, the films are homogeneously dispersed. Above that point, agglomeration of the nanoparticles may be occurring. Assuming specific gravity for the base 2P polymer and bare nanoparticles as 2.0 [2] and 1.5 [3], respectively, the 40-wt% loading is equivalent to 55% volume loading of the polymer with nanoparticles. It is quite remarkable that such high loadings are still able to produce high-quality films.

The vacuum ultraviolet transmission spectra of these films are shown in Figure 3-2 for several different nanoparticle loadings and for a neat base polymer. Two main changes in the spectrum of a neat polymer are observed with increasing loading: (1) disappearance of fringes and (2) increased transmission roll-off toward the shorter wavelengths. These changes may be caused by a combination of absorptive and scattering losses in the material. For weight loading of 40%, a substantial drop in transmission is observed at all uv wavelengths, consistent with light scattering of the spun cast film, also manifested as haziness in

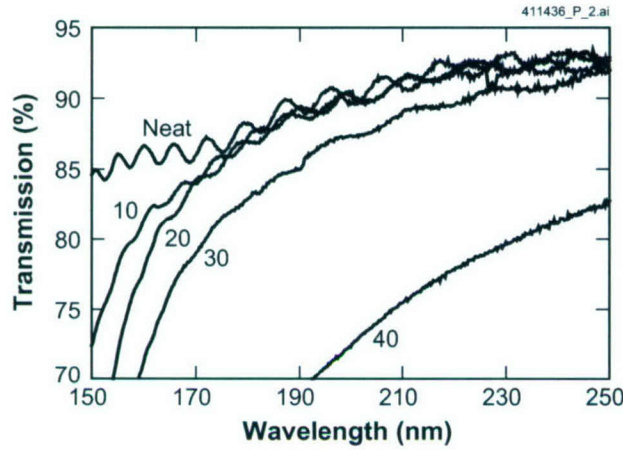


Figure 3-2. Transmission for 1- μm -thick 2P films spun cast on CaF_2 substrates. The trace labels refer to either a neat polymer ("neat") or to a polymer loaded with ST-S nanoparticles with the weight percent as indicated.

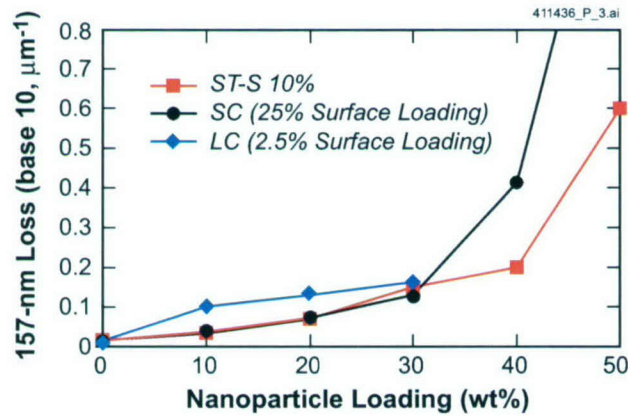


Figure 3-3. 157-nm transmission loss for bare nanoparticles and two different surface terminations.

the visible part of the spectrum. This observation is consistent with the refractive index trends of Figure 3-1, suggesting that films with $>40\%$ weight loading of nanoparticles are no longer homogeneously dispersed.

From the data of Figure 3-2, the 157-nm losses for bare nanoparticles and for the two surface terminations were computed using

$$\text{Loss} = [-\log(T_{f,157}/T_{\text{sub},157})]/d \quad (3.1)$$

with results shown in Figure 3-3.

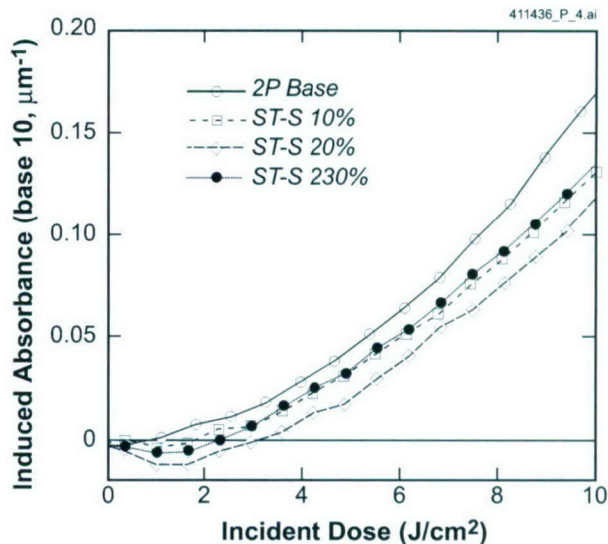


Figure 3-4. 157-nm induced absorbance in several laser-irradiated polymer films, both neat and ST-S loaded polymer.

In Equation (3.1), $T_{f,157}$ is the 157-nm transmission of the film under study, $T_{sub,157}$ is the 157-nm transmission of the CaF_2 substrate before the film was applied, and d is the thickness of the film. For a neat polymer, the loss of $0.016 \mu\text{m}^{-1}$ implies that, when the film is prepared as a $1\text{-}\mu\text{m}$ -thick freestanding pellicle, its transmission would be $\sim 96.5\%$. When nanoparticles are added to the polymer, however, the absorption increases with loading, as Figure 3-3 clearly shows. This behavior is contrary to expectations, if the nanoparticles are indeed transmissive at 157 nm. The transmission losses at 157 nm may be a combination of absorptive and scattering losses. Scattering due to the nanoparticles is expected to be very small. At 157 nm, the refractive index of the nanoparticles, assumed to be similar to that of bulk SiO_2 ($n = 1.68$), is closely matched with the refractive index of the base polymer ($n = 1.50$). Scattering caused by pinholes is also negligible, since we have not seen any evidence of void formation in the spun cast films at weight loadings below 40%. An analysis of surface roughness indicates that surface scattering contributes a relatively small loss to these films; therefore, the observed transmission losses are dominated by absorptive losses in the nanoparticles due to either impurities or defects.

Thin films of composite materials, spun cast on CaF_2 substrates, were exposed inside a purged ambient with nominal concentrations of $[\text{O}_2]$ and $[\text{H}_2\text{O}]$ of 1 and 10 ppm, respectively. A 157-nm LambdaPhysik 1020 laser was operated at 500 Hz with a fluence of $0.1 \text{ mJ/cm}^2/\text{pulse}$.

Figure 3-4 shows the induced absorbance vs incident dose for polymers loaded with varying amounts of nonfunctionalized nanoparticles. Figure 3-5, correspondingly, shows the induced absorbance

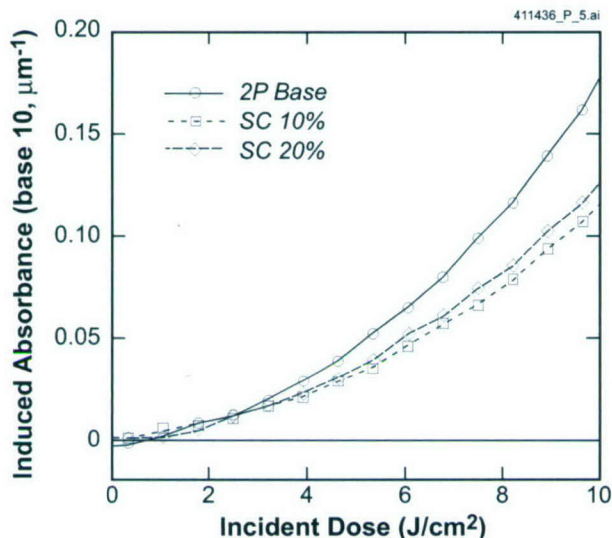


Figure 3-5. 157-nm induced absorbance in several laser-irradiated polymer films, both neat and SC-loaded polymer.

for SC functionalization of the nanoparticles. For the case of nonfunctionalized nanoparticles, the initial drop in induced absorption indicates a transmission recovery caused either by cleaning or photobleaching. For both functionalized and nonfunctionalized nanoparticle-based material, a modest reduction of photochemical darkening is observed as compared to the base polymer, $\approx 30\%$ for a 10-J/cm^2 incident dose.

The induced absorbance shown in Figures 3-4 and 3-5 was modeled using first-order rate equations; see [4] for details. From the modeling, adding a higher percentage of nanoparticles results in reduction of photodegradation via straight dilution of the absorbing centers in the original polymer. Added absorbance of the nanoparticles themselves does not appear to enhance photodegradation. No radical scavenging effects are observed—these would presumably reduce photodegradation beyond the straight dilution effects. This lack of radical scavenging is consistent with the lack of strong chemical interaction between polymer and nanoparticles that had been observed in pre-irradiation characterization.

V. Liberman	R. B. Goodman
J. H. C. Sedlacek	M. Rothschild
T. H. Fedynyshyn	R. Sinta

REFERENCES

1. R. H. French, R. C. Wheland, W. Qiu, M. F. Lemon, E. Zhang, J. Gordon, V. A. Petrov, V. F. Cherstkov, and N. I. Delaygina, *J. Fluorine Chem.* **122**, 63 (2003).

2. DuPont MSDS.
3. Calculated from www.snowtex.com/organo_types.html
4. V. Liberman, J. H. C. Sedlacek, T. H. Fedynyshyn, R. B. Goodman, M. Rothschild, and R. Sinta, to be published in *J. Microlith., Microfab., Microsyst.* **3** (2004).

4. BIOSENSOR AND MOLECULAR TECHNOLOGIES

4.1 COMPATIBILITY TESTING OF LiNK 2.0 WITH RAZOR

A sample-preparation cartridge LiNK 2.0 (Lincoln Nucleic acid Kit) has been customized for use in rapid, polymerase chain reaction (PCR) analysis of DNA [1]. This cartridge, which was designed for compatibility with the RAZOR instrument (Idaho Technology), is field-deployable, requires no power or additional reagents, and has a total processing time of 6 min. Here, we report the testing of LiNK 2.0 with RAZOR against two targets, Ba spores and Btk spores, in three different matrices: growth media, dirty environmental water, and acid-washed sand.

The LiNK 2.0 in combination with the RAZOR was shown to detect Ba and Btk spores in all three matrices of interest, with a success rate of 100% for high concentrations (1×10^6 cfu/mL) and 50–66% at a lower concentration (1×10^3 cfu/mL). These success rates were shown to be comparable to that of a benchtop “gold standard” that processes samples with the simple nucleic acid preparation (SNAP) and then analyzes them with a laboratory-grade ABI 7700 PCR machine.

Throughout the validation experiments the syringe loading mechanism behaved as expected. When a 2-mL elution volume was used, two RAZOR sample ports could be loaded from a single LiNK 2.0 without introduction of bubbles into the RAZOR pouch. In addition, the LiNK 2.0 was shown not to leak under depressurization and tolerated a temperature range from -20 to 85°C .

Both Ba and Btk spores were produced at Lincoln Laboratory using standard protocols. Nutrient-deficient media were spiked with overnight culture of either Ba or Btk and allowed to incubate at 37°C for 48 h. The cultures were washed a minimum of five times to remove extraneous DNA and then incubated at 60°C for 60 min to ensure that no vegetative cells survived. Spore suspensions were quantified by counting colonies on plates streaked with sample and stored at 4°C . To create sand samples, acid-washed sand was purchased from VWR International and spiked with either Ba or Btk spore by adding spore-containing liquid to sand and allowing the wet sand to dry at room temperature for 48 h.

For all the experiments described below, spiked samples were processed with the LiNK 2.0 and then run in a RAZOR. The LiNK 2.0 eluates were also run with an ABI 7700 using TaqMan chemistries, as were the spiked samples without processing. Because of the additional 1:10 dilution required to prepare samples for the ABI 7700, it was expected that processing LiNK 2.0 eluates with the ABI 7700 would have later cycle thresholds (CTs) and might not detect as many samples at the lower concentrations. Spiked samples were also processed with SNAP and analyzed with the ABI 7700 to provide a benchmark to which the RAZOR results could be compared; these samples are referred to as ABI.

In real-time PCR, the CT is typically used to determine if a sample is positive, negative, or unclear. For the RAZOR results, the CT values generated by RAZOR were used. For the ABI 7700, the CT value for each curve was defined as the cycle at which the curve crossed a normalized fluorescence value of 0.1. In addition, the curve had to exhibit exponential behavior prior to crossing 0.1.

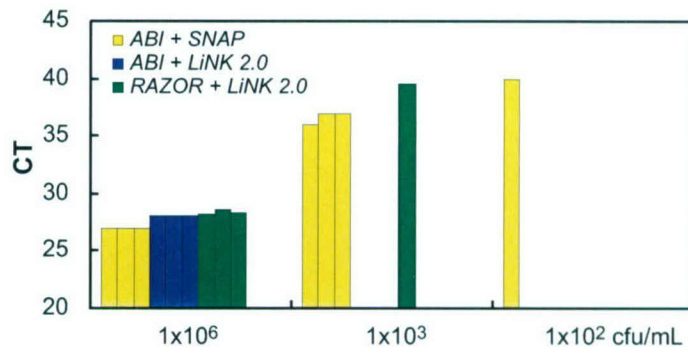


Figure 4-1. Results of assay for *Ba* spore in dirty water.

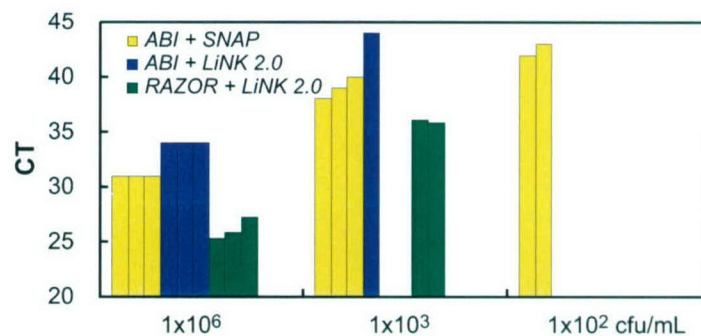


Figure 4-2. Results of assay for *Btk* spore in dirty water.

The design of the RAZOR pouch, in which a single liquid sample enters three different assay chambers, affected the approach to the data analysis. For *Btk*, each assay chamber tests for the same PCR target; therefore, the sample results are shown as an average of three CT values. In contrast, for *Ba*, the three assay chambers test for three different PCR targets (chromosomal DNA, plasmid pXO1 DNA, and plasmid pXO2 DNA). All three components are necessary for the *Ba* to be pathogenic. The *Ba* results are reported therefore as individual CT values. The ABI 7700 *Ba* assay tests only for pXO1.

All three analyses (ABI + SNAP, ABI + LiNK 2.0, RAZOR + LiNK 2.0) were run at both high and low concentrations for both targets in all three matrices. “Missing” bars from the graphs in the figures therefore indicate that a sample was run but was negative.

The “dirty water” samples, shown in Figures 4-1 and 4-2, were the first to be included in the LiNK 2.0 validation; therefore, two low concentrations were tested to determine which to use for the remaining validations. Since none of the *Btk* samples or *Ba* samples gave clear positive results for 1×10^2 cfu/mL

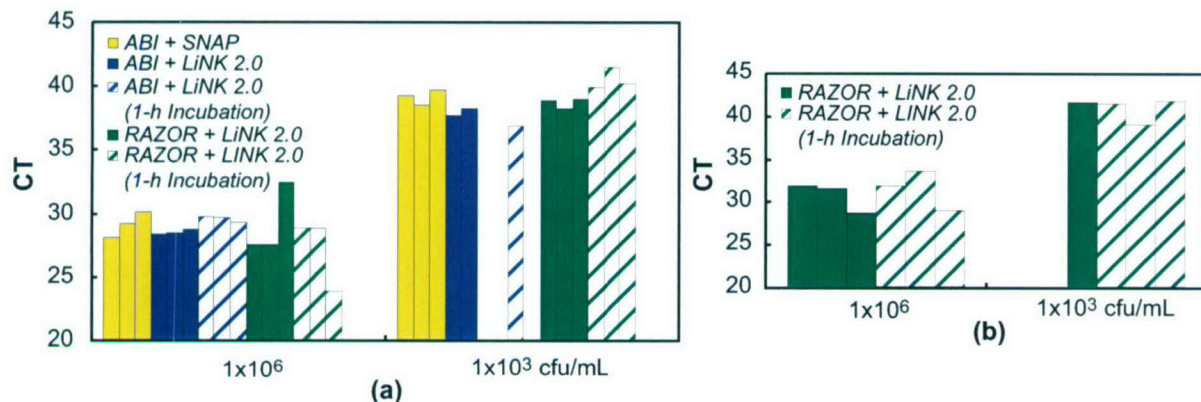


Figure 4-3. Results of assay for *Ba* spore in Leighton-Doi growth media: (a) pXOI target and (b) chromosomal target (RAZOR data only).

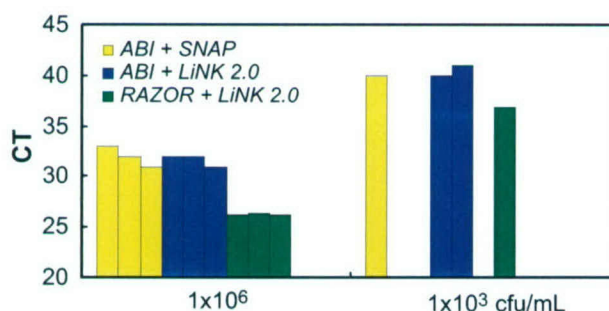


Figure 4-4. Results of assay for *Btk* spore in Leighton-Doi growth media.

when analyzed with the RAZOR, it was decided to use 1×10^3 cfu/ml as the low concentration. Analysis with ABI 7700 + SNAP yielded detection at 1×10^2 cfu/mL, at one out of three for *Ba* and two out of three for *Btk*. The RAZOR + LiNK 2.0 method performed as well as the ABI 7700 + SNAP gold standard in terms of percentage of samples detected at the high concentration but had a lower rate of detection at the lower concentrations.

For Leighton-Doi (LD) growth media, shown in Figures 4-3 and 4-4, an additional parameter was examined: the time the sample is allowed to incubate on the end of the LiNK 2.0 prior to eluting into the inner chamber of the LiNK 2.0 body. The standard procedure calls for 5 min, but when processing large numbers of LiNK 2.0 devices, this time may vary from sample to sample. One of the validation laboratories had requested that this potential variance be examined. The effect of increasing the

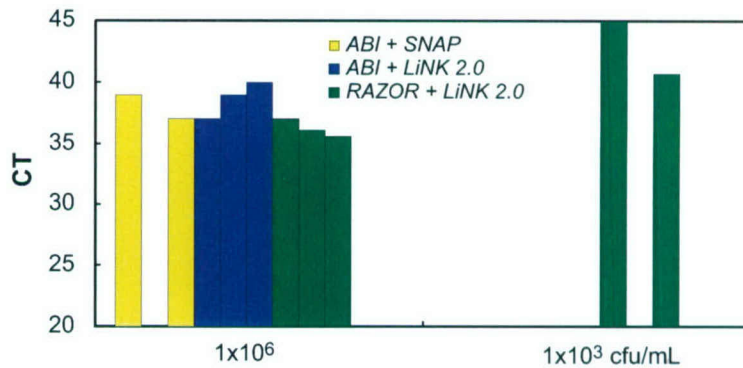


Figure 4-5. Results of assay for Ba spore in sand.

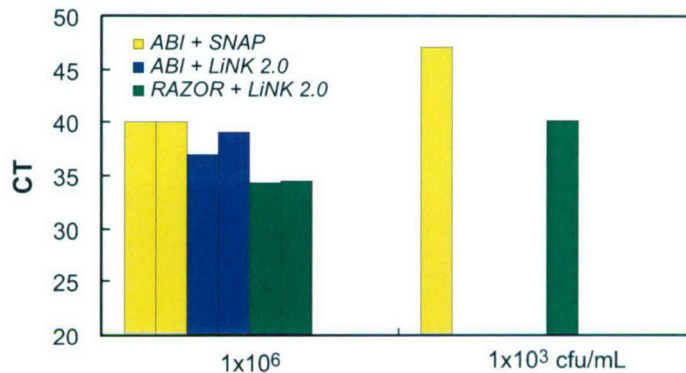


Figure 4-6. Results of assay for Btk spore in sand.

incubation time does not appear to be significant for the pXO1 target but did appear to improve the percentage of low-concentration samples detected with the chromosomal target, as seen in Figure 4-3. The effect on Btk detection was not tested. The RAZOR + LiNK 2.0 method performed as well as the ABI 7700 + SNAP in terms of percentage of samples detected at the high and low concentrations.

Results for sand are shown in Figures 4-5 and 4-6. With sand, as with the LD growth media, the ABI 7700 + SNAP and RAZOR + LiNK 2.0 approaches gave comparable results in terms of detection of target at low concentrations. Although the LiNK 2.0 method appeared to detect two out of three low-concentration Ba samples while the SNAP method did not detect any at that concentration, the lack of positive results from the chromosomal target channel, as seen in Figure 4-5, makes this comparison problematic. For example, if a Ba sample is positive for pXO1 but not for the chromosomal target, that sample could be classified either as positive for Ba or inconclusive and requiring confirmatory testing.

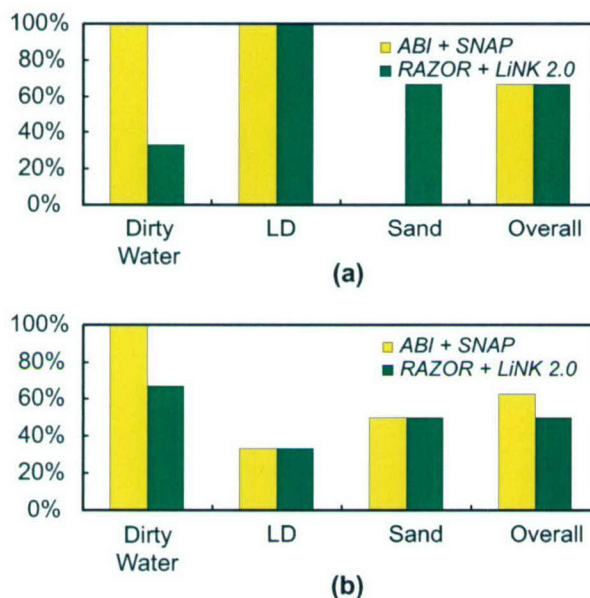


Figure 4-7. Comparison between ABI 7700 + SNAP and RAZOR + LiNK 2.0 for detection of (a) *Ba* spore at 1×10^3 cfu/mL and (b) *Btk* spore at 1×10^3 cfu/mL.

Even for *Btk*, with the same target in all three lanes, samples occasionally register positive for two out of three lanes, which again could be classified as either positive or requiring additional analysis. The RAZOR + LiNK 2.0 method performed as well as, if not better than, the ABI 7700 + SNAP in terms of percentage of samples detected at the high and low concentrations.

Thus, all high-concentration samples were detected using the RAZOR + LiNK 2.0 approach. Approximately 66% of the *Ba* low-concentration samples and 50% of the *Btk* low-concentration samples were detected using the RAZOR + LiNK 2.0. LiNK 2.0 eluates analyzed with the ABI 7700 did not perform as well as when analyzed with the RAZOR, which was expected given the 1:10 dilution required to run samples on the ABI 7700. More important, the LiNK 2.0 eluates that were analyzed with the ABI 7700 did not produce any positive results that the RAZOR analysis missed.

Overall, at high concentrations the RAZOR + LiNK 2.0 performed as well as or better than the ABI 7700 + SNAP gold standard. For high concentrations (1×10^6 cfu/mL) spiked into dirty water and LD media, the RAZOR + LiNK 2.0 protocol performed as well as the gold standard ABI 7700 + SNAP, as both methods successfully detected 100% of the samples. The RAZOR + LiNK 2.0 protocol actually performed better than the gold standard for sandy soils, detecting 100% of the spiked samples while the ABI 7700 + SNAP missed one of the *Ba*-spiked sand samples, as seen Figure 4-6.

Compared with the gold standard, at low concentrations the RAZOR + LiNK 2.0 performance varied with the environmental matrix tested but overall did nearly as well as the gold standard and in one case

better, as shown in Figure 4-7. For low concentrations (1×10^3 cfu/mL) spiked into LD media, the RAZOR + LiNK 2.0 performed as well as the ABI 7700 + SNAP. In dirty water at low spiked concentrations, the RAZOR + LiNK 2.0 did not perform quite as well as the gold standard, i.e., three of three times for ABI 7700 + SNAP for both targets vs one of three times for Ba and two of three times for Btk for RAZOR + LiNK 2.0. For sandy soils, the RAZOR + LiNK 2.0 outperformed the ABI 7700 + SNAP, particularly for the Ba-spiked samples, which were detected two out of three times with the RAZOR + LiNK 2.0 but not detected at all by the gold standard protocol, as seen in Figure 4-6. ABI 7700 + SNAP did detect target at one order of magnitude more dilute than the working low concentration in one matrix, dirty water.

In conclusion, a set of validation experiments was performed in which LiNK 2.0 cartridges and a RAZOR PCR machine were used to process environmental samples containing biological agent simulant. All samples spiked to a concentration of 1×10^6 cfu/mL were successfully detected as positive. At a lower concentration of 1×10^3 cfu/mL, 66% of Ba-spiked samples and 50% of Btk-spiked samples were successfully detected as positive. These results were compared to those of a laboratory-grade gold standard ABI 7700 + SNAP analysis method. With the exception of spore detection at low concentrations in dirty water, which was 50% for RAZOR + LiNK 2.0 vs 100% for the gold standard, the RAZOR + LiNK 2.0 procedure was found to be overall as effective as the gold standard DNA detection method, and for sand samples more effective.

C. R. Cabrera

REFERENCE

1. Solid State Research Report, Lincoln Laboratory, MIT, 2004:2, p. 25.

5. ADVANCED IMAGING TECHNOLOGY

5.1 ORTHOGONAL-TRANSFER ARRAY FOR ADAPTIVE IMAGING IN ASTRONOMY

Ground-based astronomy must contend with the optical phase distortions arising from atmospheric winds and turbulence that reduce resolution to well below the diffraction limit of large telescopes. The orthogonal-transfer charge-coupled device (OTCCD) has been shown to be effective in dealing with the lowest-order mode of these distortions, namely, simple wavefront tilt. The ability of the OTCCD to shift charge in all directions has enabled it to be used to perform the so-called tip-tilt correction electronically by shifting the integrated charge pattern in synchronism with the image motion [1]. The wavefront tilt, however, is correlated only over a patch of sky characterized by the isoplanatic angle, which is typically a few arc minutes. For imaging over a field of view wider than this angle, a single correction becomes less effective. In this case, multiple OTCCDs, each viewing an area smaller than the isoplanatic patch and driven by an independent correction appropriate to the local wavefront tilt, must be used. We describe here a new architecture, called the orthogonal-transfer array (OTA), that addresses the use of OTCCDs for wide-field imaging. Prototype devices have been designed and fabricated for the Pan-STARRS (Panoramic Survey Telescope and Rapid Response System) program at the University of Hawaii under Air Force sponsorship [2].

Figure 5-1 illustrates the basic building blocks of the OTA. The detector consists of an 8×8 array of OTCCD subarrays or cells, shown in Figure 5-1(a), each cell in turn comprising an array of about 500×500 pixels, shown in Figure 5-1(b), and a serial readout register. The pixels are four-phase OTCCD structures with one of the two pixel designs shown in Figure 5-1(c). Associated with each OTA cell is a

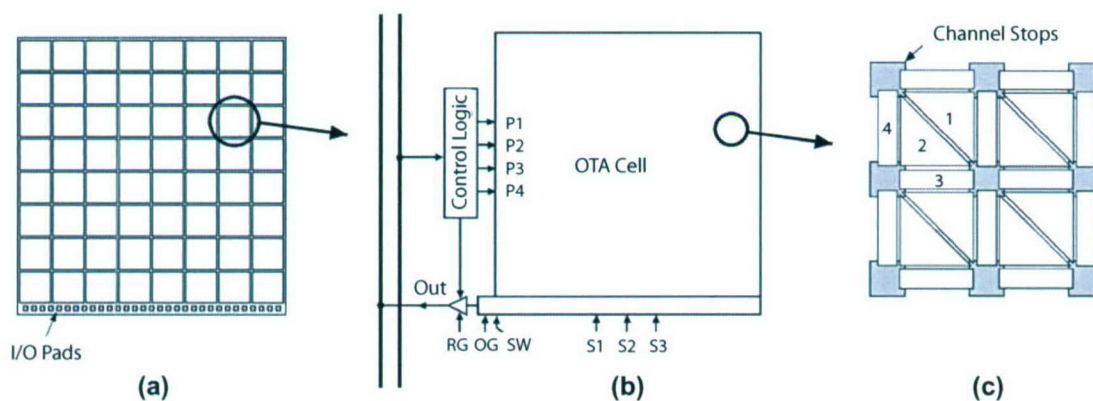


Figure 5-1. Principal elements of the orthogonal transfer array (OTA): (a) Overall chip layout comprising an 8×8 array of OTCCD cells, (b) OTA cell with its control logic, and (c) one of the OTCCD pixel geometries.

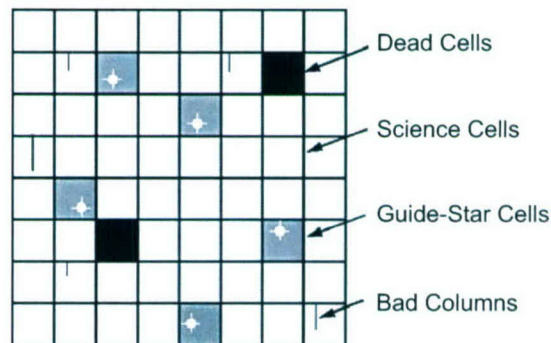


Figure 5-2. Depiction of OTA operation.

control-logic block that is used to control the four parallel phases, P1–P4, and the video output signal of each cell. Each logic block can be addressed and loaded with data bits that (1) determine whether the parallel clocks are stationary (during integration) or shifting charge, and (2) enable/disable the output-amplifier connection to the video output bus. These features are described in more detail later. To maximize fill factor, the cells are abutted as closely as permitted by the process technology, and all I/O leads are confined to one edge of the device. The die size is 49.5×49.5 mm, a size chosen on the basis that a 150-mm wafer can just accommodate four such devices.

The operation of the OTA has been described [3] and will be reviewed here with the help of Figure 5-2. All functioning cells are assigned either to image guide stars for measuring the local image translation or to acquire the science images. Some cells will inevitably be nonfunctional, but the gaps in the science imagery arising from these, as well as the other nonactive regions of the focal plane and the guide star cells, will be filled in by the usual strategy in astronomical imaging of stacking a set of dithered images.

The first step in imaging a sector of sky is to select those cells, perhaps four or five, that happen to contain sufficiently bright stars to be used as guide stars. These cells will image and read out a small subarray of pixels around the guide star, and from this data the centroids of the stars will be used to construct a map of the image deflection field over the chip field of view. “Sufficiently bright” thus means stars that will yield imagery of sufficient signal-to-noise ratio to enable reasonably precise centroiding. This information, in turn, is used to address and update the science cells with the appropriate pixel shifts. The nominal rate at which the cycle of guide-star read and science-cell update occurs is 30 Hz. At the conclusion of the integration period the cells are read out one row at a time through eight video lines that service the eight cells in each column.

Figure 5-3 illustrates the control and readout lines and the logic block associated with each cell. When a logic cell is selected by asserting the corresponding row and column select lines, three data bits, D0–D2, are latched into the cell. These bits set the state of three output control bits, Z0–Z2, which control

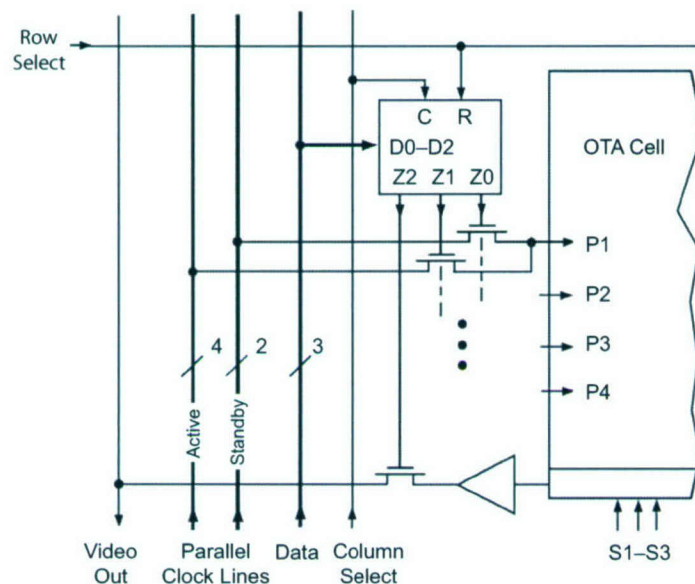


Figure 5-3. Arrangement of control lines and logic for each OTA cell.

a set of pass transistors. Bits Z0 and Z1 determine whether each parallel clock phase is set to an active clock line for charge transfer or to one of two standby levels (high, low) during image acquisition. Both bits can be set low to disconnect these gates entirely from the clock lines, a feature that will prove useful for dealing with cells that have serious gate shorts. Such shorts might otherwise place a severe load on the clock lines or inject large amounts of charge into the substrate.

The Z2 bits determine which output video signals are multiplexed onto each of eight column video-out lines. Because all the cells in a column share a single video-out bus, we are constrained to reading only one cell per column at a time. The design goal for the serial read rate is 1.0 MHz, which combined with the relatively long video-output lines requires a two-stage source follower for the CCD output amplifier.

In order to add the required circuitry with no reduction in imaging performance and maintain the simplest wafer fabrication process, we elected to use NMOS logic. This type of logic was in wide use until the end of the 1970s when its high power consumption led to its replacement by CMOS. In the OTA the transistor count is sufficiently low that the NMOS power dissipation is manageable. Of major importance is the fact that NMOS can be added to an *n*-channel CCD process with very little additional process overhead. Typically, only one or two additional ion-implant steps are required, provided the logic devices can perform satisfactorily with the same gate dielectric thicknesses and substrate resistivity as the CCD. The latter requirement is particularly critical, since the CCD must be made on high-resistivity substrates

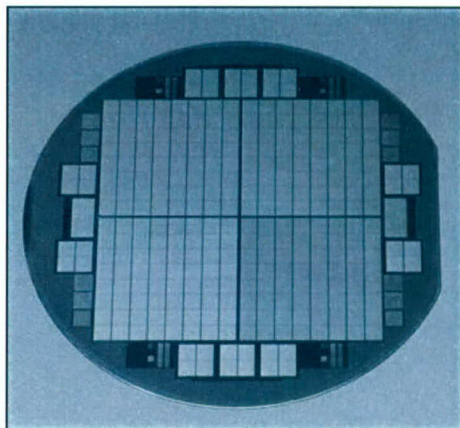


Figure 5-4. Photograph of completed wafer showing four large OTAs surrounded by smaller versions of OTAs (2×2 cells), a standard three-phase imager, and process control cells.

($\sim 5000\text{--}10,000 \Omega\cdot\text{cm}$) to enable deep depletion layers for enhanced near-infrared response. We find that NMOS can be made compatible with such material provided the channel lengths are $4 \mu\text{m}$ or longer.

The first lot of prototype devices has just been completed and is now undergoing testing. Figure 5-4 is a photograph of one of the wafers and shows the four large OTAs surrounded by smaller test imagers, including eight small OTAs or mini-OTAs (MOTAs) comprising 2×2 cells. All the OTAs and MOTAs feature a variety of pixel designs, pixel sizes, and other design variations, which will be studied before a final design is chosen for the Pan-STARRS focal-plane arrays.

B. E. Burke	M. Cooper
D. Young	J. Tonry*

REFERENCES

1. J. L. Tonry, B. E. Burke, and P. L. Schechter, *PASP* **109**, 1154 (1997).
2. N. Kaiser, H. Aussel, B. Burke, et al., *Proc. SPIE* **4836**, 154 (2002).
3. J. L. Tonry, G. A. Luppino, N. Kaiser, B. E. Burke, and G. H. Jacoby, *Proc. SPIE* **4836**, 206 (2002).

*Author not at Lincoln Laboratory.

6. ANALOG DEVICE TECHNOLOGY

6.1 ELECTROMAGNETICALLY INDUCED TRANSPARENCY WITH SUPERCONDUCTIVE QUANTUM CIRCUITS

Superconductive quantum circuits (SQC) comprising mesoscopic Josephson junctions can exhibit quantum coherence amongst their macroscopic degrees of freedom under carefully controlled experimental conditions [1]. They feature quantized flux and/or charge states depending on their fabrication parameters, and the resultant quantized energy levels are analogous to the quantized internal levels of an atom. Spectroscopy, Rabi oscillation, and Ramsey interferometry, experimental phenomena often associated with atomic and nuclear systems, have recently been realized with SQCs designed to behave as “artificial atoms” [2]–[10].

This leads one to an interesting question: Can SQCs exhibit other quantum optical effects associated with atomic systems? We address here one such example by extending the SQC-atom analogy to another quantum optical effect associated with atoms: electromagnetically induced transparency (EIT) [11],[12]. We propose the demonstration of microwave transparency using a superconductive analog to EIT (denoted S-EIT) in a superconductive circuit exhibiting two metastable states, e.g., a qubit, and a third, shorter-lived state, e.g., the readout state [13].

The three-level Λ -system illustrated in Figure 6-1(a) is a standard energy-level configuration utilized in EIT; it comprises two metastable states $|1\rangle$ and $|2\rangle$, each of which may be coupled to a third excited state $|3\rangle$ [11],[12]. In atoms, the metastable states are typically hyperfine or Zeeman levels, while state $|3\rangle$ is an excited electronic state that may spontaneously decay at a relatively fast rate Γ_3 . In Figure 6-1(b), the electromagnetic field from laser 1 is tuned to be resonant with the $|1\rangle \rightarrow |3\rangle$ transition. When it is solely radiating the device, it can coherently drive population from state $|1\rangle$ to $|3\rangle$; such transitions correspond to the absorption of photon(s). Similarly, as shown in Figure 6-1(c), the electromagnetic field from laser 2 is tuned to the $|2\rangle \rightarrow |3\rangle$ transition, and when it alone radiates the Λ -system, the result is a population transfer from state $|2\rangle$ to $|3\rangle$ as mediated by the absorption of photon(s). The transition coupling strengths are characterized by their Rabi frequencies $\Omega_{j3} = \vec{d}_{j3} \cdot \vec{E}_{j3}$ for $j = 1, 2$, respectively, in which \vec{d}_{j3} are the dipole matrix elements and \vec{E}_{j3} are the slowly varying envelopes of the applied electric fields. The Rabi frequency establishes the rate at which the transitions occur, and it is proportional to the electric field amplitude. As intuition dictates, larger amplitudes result in faster transitions. In general, population driven to state $|3\rangle$ can spontaneously decay to states within or external to the Λ -system, or it can be coherently driven back to states $|j\rangle$. Here, for simplicity, we will assume that the spontaneous decay rate Γ_3 to states outside the Λ -system is much larger than the Rabi frequencies Ω_{j3} .

EIT is a quantum interference effect in which the absorption of photons from two simultaneously applied electromagnetic fields is prevented, even though absorption would occur for each field applied independently as in Figures 6-1(b) and 6-1(c). For particular Rabi frequencies Ω_{j3} , the simultaneous

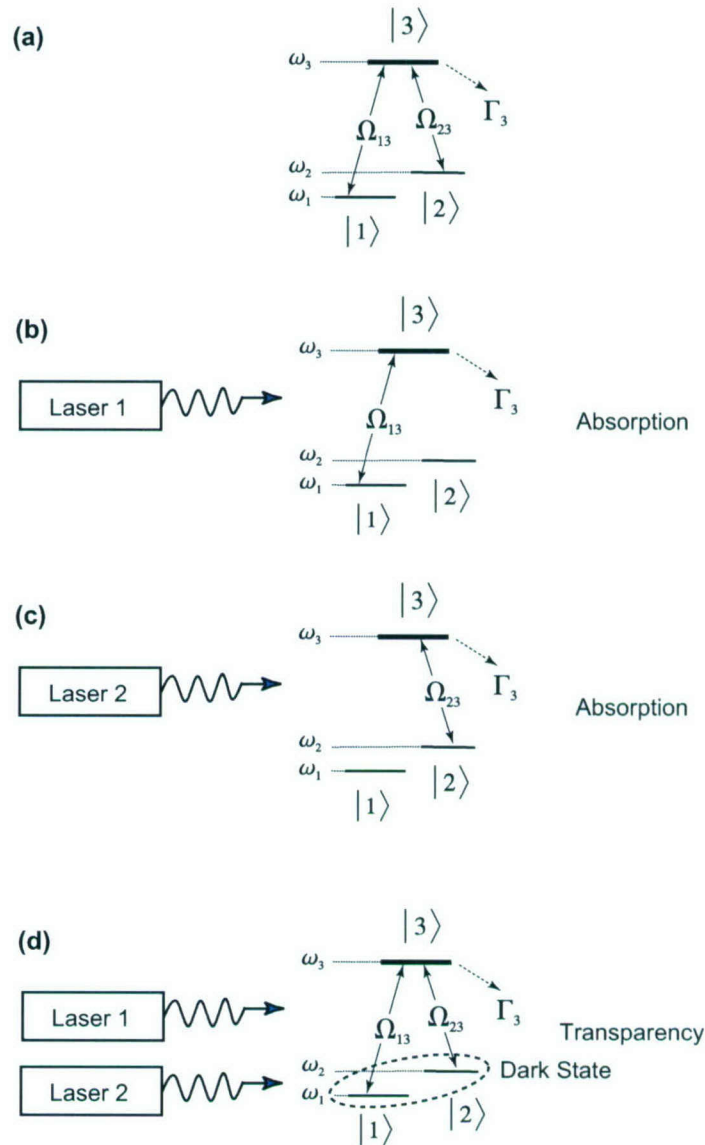


Figure 6-1. (a) Atomic A-system. Levels 1 and 2 are taken to be metastable, and level 3 decays primarily to levels outside the system at a rate Γ_3 . ω_i are the frequencies of the levels (energy in rad/sec). Ω_{ij} are the Rabi frequencies used to represent the field strengths of the driven transitions. (b) Radiation drives the $1 \rightarrow 3$ transition. Population in level 1 is transferred to level 3 by the absorption of photons, where it is assumed to decay via the Γ_3 channels. (c) Radiation drives the $2 \rightarrow 3$ transition. Population in level 2 is transferred to level 3 by the absorption of photons, where it is assumed to decay via the Γ_3 channels. (d) If the system is prepared in a dark state, the simultaneous application of radiation fields Ω_{13} and Ω_{23} results in electromagnetically induced transparency; no photon absorption occurs owing to a destructive quantum interference of the two driven transitions. As a result, population remains in the dark state (levels 1 and 2).

application of the two electromagnetic fields, e.g., lasers 1 and 2 as in Figure 6-1(d), decouples both fields from the atomic system through a destructive quantum interference of the two driven transitions. The result is a suppression of the photon absorption from both fields, and the atomic system becomes transparent to these fields. Although outside the scope of this report, EIT also generates refractive-index modifications that can result in ultraslow light propagation [14]–[16].

SQCs also exhibit Λ -like energy level structures [7],[17]–[22]. One example is the persistent-current (PC) qubit, a superconductive loop interrupted by two Josephson junctions of equal size and a third junction scaled smaller in area by the factor $\alpha < 1$, as seen in Figure 6-2(a) [23],[24]. Its dynamics are described by the Hamiltonian

$$H_{\text{PC}} = \frac{1}{2} C \left(\frac{\Phi_0}{2\pi} \right)^2 \left(\dot{\varphi}_p^2 + (1 + 2\alpha) \dot{\varphi}_m^2 \right) + E_J \left[2 + \alpha - 2 \cos \varphi_p \cos \varphi_m - \alpha \cos(2\pi f + 2\varphi_m) \right] \quad (6.1)$$

in which C is the capacitance of the larger junctions, $\varphi_{p,m} \equiv (\varphi_1 \pm \varphi_2)/2$, φ_i is the gauge-invariant phase across the larger junctions $i = \{1, 2\}$, E_J is the Josephson coupling energy, and f is the magnetic flux through the loop in units of the flux quantum Φ_0 [23]. Near $f \approx 1/2$, the qubit potential landscape, i.e., the second term in Equation (6.1), assumes a double-well profile. Each well corresponds to a distinct classical state of the electric current, i.e., left or right circulation about the qubit loop, and its net magnetization is discernable using a dc superconducting quantum interference device (SQUID) [23],[24]. As a quantum object, the potential wells exhibit quantized energy levels corresponding to the quantum states of the macroscopic circulating current [17],[18]. These levels may be coupled using microwave radiation [4],[19], and their quantum coherence has been experimentally demonstrated [8].

Tuning the flux bias away from $f = 1/2$ results in the asymmetric double-well potential illustrated in Figure 6-2(b). The three states in the left well constitute the superconductive analog to the atomic Λ -system. Using tight-binding models with experimental PC qubit parameters [18],[19],[23] at a flux bias $f = 0.504$, we estimate the interwell resonant-tunneling rates for states $|1\rangle$, $|2\rangle$, and $|3\rangle$ to be $\Gamma_1^{\text{r}} \approx 1 \text{ ms}^{-1}$, $\Gamma_2^{\text{r}} \approx 1 \text{ } \mu\text{s}^{-1}$, and $\Gamma_3^{\text{r}} \approx 1 \text{ ns}^{-1}$ respectively. An off-resonant biasing of state $|3\rangle$ decreases its interwell tunneling rate to order $100 \text{ } \mu\text{s}$; the off-resonant biasing of states $|1\rangle$ and $|2\rangle$, as in Figure 6-2(b), will also significantly decrease their interwell tunneling rates. In addition, the intrawell relaxation rate at a similar flux bias was experimentally determined to be $\Gamma_3^{(\text{intra})} \approx 25 \text{ } \mu\text{s}^{-1}$ and, presumably, $\Gamma_2^{(\text{intra})} < \Gamma_3^{(\text{intra})}$. Therefore, the “qubit states” $|1\rangle$ and $|2\rangle$ are effectively metastable with respect to the resonantly biased “readout state” $|3\rangle$. Since $\Gamma_3^{(\text{r})} \gg \Gamma_3^{(\text{intra})}$ [17]–[19], a particle reaching state $|3\rangle$ will tunnel quickly to state $|4\rangle$, an event that is detectable by a dc SQUID. Alternatively, for slower detection schemes, one may detune states $|3\rangle$ and $|4\rangle$, and then apply a resonant π -pulse to transfer the population from states $|3\rangle$ and $|4\rangle$.

Transitions between the quantized levels are driven by resonant microwave-frequency magnetic fields. By assuming the Rabi frequencies Ω_{ij} to be much smaller than all level spacings $\omega_{kl} \equiv |\omega_k - \omega_l|$, the system-field interaction may be written within the rotating wave approximation (RWA)

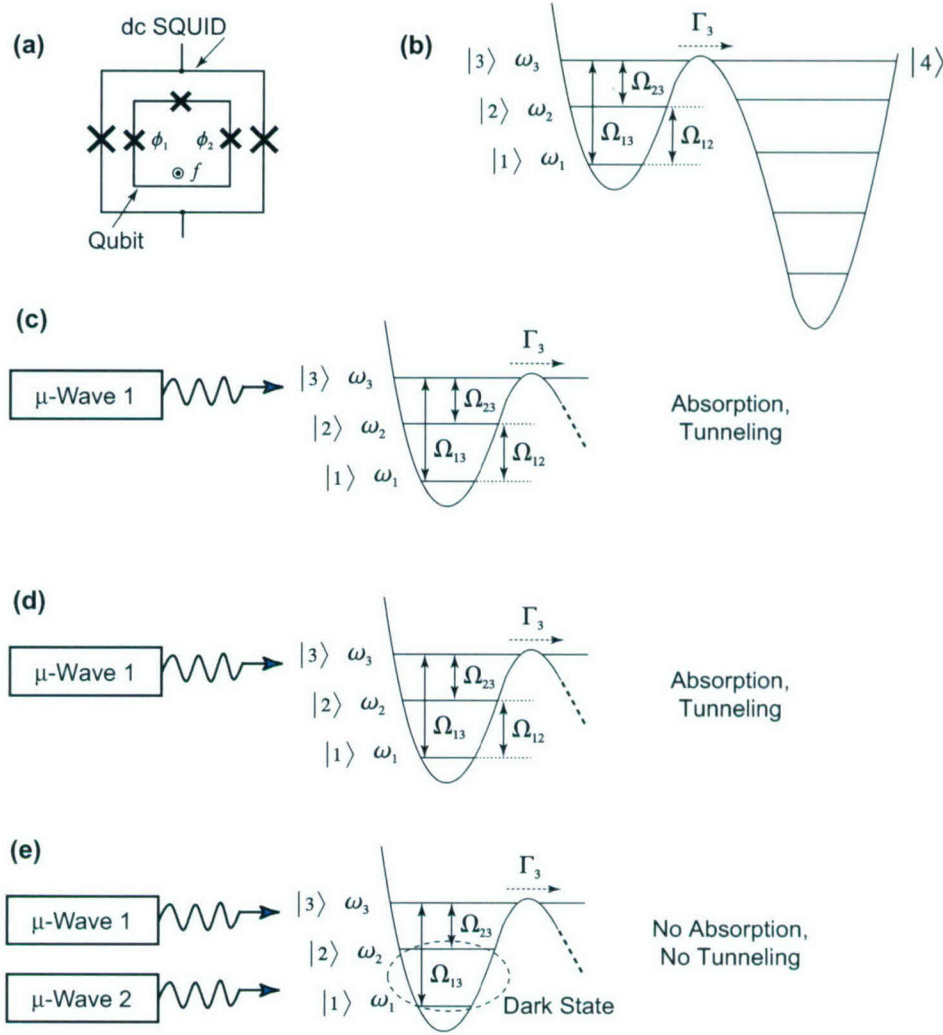


Figure 6-2. (a) Superconductive flux qubit and superconducting quantum interference device (SQUID). ϕ_1 and ϕ_2 are the gauge-invariant phases of the larger-two qubit junctions. An applied flux f tunes the potential landscape of the qubit. (b) Asymmetric double-well potential of the flux qubit at a bias point $f = 0.504$. The three levels in the left well constitute the Λ -system. Tunneling to the right well can be observed by the SQUID. (c) Microwave radiation drives the $1 \rightarrow 3$ transition. Population in level 1 is transferred to level 3 by the absorption of photons, where it quickly tunnels to the right well and is detected by the SQUID. (d) Microwave radiation drives the $2 \rightarrow 3$ transition. Population in level 2 is transferred to level 3 by the absorption of photons, where it quickly tunnels to the right well and is detected by the SQUID. (e) If the qubit is prepared in a dark state, the simultaneous application of microwave fields Ω_{13} and Ω_{23} results in EIT; no photon absorption occurs because of a destructive quantum interference of the two driven transitions. As a result, population remains in the dark state (levels 1 and 2). Since no population reaches state $|3\rangle$, the SQUID does not detect a tunneling event.

$$H_{\text{int}}^{(\text{RWA})} = \frac{\hbar}{2} \begin{pmatrix} 0 & \Omega_{12}^* & \Omega_{13}^* \\ \Omega_{12} & 0 & \Omega_{23}^* \\ \Omega_{13} & \Omega_{23} & -i\Gamma_3 \end{pmatrix} \quad (6.2)$$

in which the decay from state $|3\rangle$ is treated phenomenologically as a non-Hermitian matrix element [25],[26]. For small microwave perturbations of the frustration, Δf , the associated Rabi frequencies are

$$\Omega_{pq} = 2\pi\Delta f \left(\frac{\alpha E_J}{\hbar} \right) \langle p | \sin(2\pi f + 2\varphi_m) | q \rangle ; \quad (6.3)$$

numerical simulations of the matrix elements are consistent with recent experimental results [17]–[19]. A qubit initially in state $|1\rangle$ can be read out by applying a microwave field Ω_{13} , which drives the $1 \rightarrow 3$ transition through photon absorption, as seen in Figure 6-2(c). Readout occurs when the population in state $|3\rangle$ quickly tunnels to the right well. Similarly, a qubit initially in state $|2\rangle$ can be read out by applying a microwave field Ω_{23} and driving the $2 \rightarrow 3$ transition, as seen in Figure 6-2(d). Furthermore, a qubit can be prepared in a superposition state $|\Psi\rangle = c_1|1\rangle + c_2|2\rangle$ by temporarily driving the Ω_{12} field, as seen in Figure 6-2(b). Applying the Ω_{13} (Ω_{23}) field then allows the population of state $|1\rangle$ ($|2\rangle$) to be read out through a transition to state $|3\rangle$ followed by a rapid escape to the right well. This type of readout scheme is also utilized for single-junction qubits [7]. As with the atomic system, these single-field transitions to state $|3\rangle$ require photon absorption.

Alternatively, one may achieve S-EITs in a superconductive Λ -system that is prepared in state $|\Psi\rangle$ by simultaneously applying the microwave fields Ω_{13} and Ω_{23} , as seen in Figure 6-2(e), such that

$$\frac{\Omega_{13}}{\Omega_{23}} = -\frac{c_2}{c_1} \quad (6.4)$$

Under this condition (with $\Omega_{12} = 0$), the state $|\Psi\rangle$ is an eigenstate of $H_{\text{int}}^{(\text{RWA})}$ in Equation (6.2) with eigenvalue zero; in this “dark state,” the SQC becomes transparent to the microwave fields. As in conventional EIT, the amplitudes for the two absorptive transitions into $|3\rangle$ have equal and opposite probability amplitudes, leading to a destructive quantum interference and no population loss through the readout state $|3\rangle$. Thus, S-EIT provides a means to confirm, without disturbing the system, that one had indeed prepared the qubit in a dark state.

S-EIT may ultimately be useful in the characterization of decoherence in superconductive qubits. In a practical SQC, there will be imperfect preparation as well as decoherence of the state $|\Psi\rangle$, and this must be measured, characterized, and minimized for quantum information applications. S-EIT is a sensitive probe for this purpose, since deviations in the amplitude and/or relative phase of the complex coefficients c_i from the condition established in Equation (6.4) result in a small probability

$$\frac{|c_1\Omega_{13} + c_2\Omega_{23}|^2}{\sqrt{|\Omega_{13}|^2 + |\Omega_{23}|^2}} \quad (6.5)$$

of the SQC being driven into the readout state $|3\rangle$ on a time scale $\sim \Gamma_3 / \sqrt{|\Omega_{13}|^2 + |\Omega_{23}|^2}$. This application is not unique; for example, decoherence may also be monitored by Ramsey interferometry. However, S-EIT may provide a more sensitive means to characterize this decoherence, as even small deviations from the dark state can drive a measurable population to the readout state. Furthermore, the dark states are prototypical qubit states that are used as resources in quantum computation. S-EIT can be used as a reliability measure to confirm that the qubit state in fact remains in a particular dark state if no population transition is observed. This aspect of S-EIT is unique. Further details of the analysis and application of S-EIT can be found in [13].

In conclusion, we have proposed using the superconductive analog to EIT, S-EIT, to demonstrate macroscopic quantum interference in SQCs. We have shown how S-EIT can be used to measure, with a single pulse of the two S-EIT fields, whether a particular superposition of metastable energy levels (a qubit) has been prepared. The technique is distinguishable from previous state measurement schemes [7] in that S-EIT ideally does not disturb the system, preserving its quantum coherence when it has been prepared in the desired state. Furthermore, we have described how S-EIT can very sensitively probe small qubit errors due to decoherence or imperfect state preparation. We have obtained elsewhere [13] analytic expressions for the field strengths required to measure the qubit dephasing rate.

W. D. Oliver	K. Murali*
Z. Dutton*	T. P. Orlando*

REFERENCES

1. A. J. Leggett and A. Gard, *Phys. Rev. Lett.* **54**, 857 (1985).
2. Y. Nakamura, Y. A. Pashkin, and J. S. Tsai, *Nature (London)* **398**, 786 (1999); Y. A. Pashkin, T. Yamamoto, O. Astafiev, Y. Nakamura, D. V. Averin, and J. S. Tsai, *Nature (London)* **421**, 823 (2003).
3. J. R. Friedman, V. Patel, W. Chen, S. K. Tolpygo, and J. E. Lukens, *Nature (London)* **406**, 43 (2000).
4. C. H. van der Wal, A. C. J. ter Haar, F. K. Wilhelm, R. N. Schouten, C. J. P. M. Harmans, T. P. Orlando, S. Lloyd, and J. E. Mooij, *Science* **290**, 773 (2000).

*Author not at Lincoln Laboratory.

5. D. Vion, A. Aassime, A. Cottet, P. Joyez, H. Pothier, C. Urbina, D. Esteve, and M. H. Devoret, *Science* **296**, 886 (2002).
6. Y. Yu, S. Han, X. Chu, S.-I. Chu, and Z. Wang, *Science* **296**, 889 (2002).
7. J. M. Martinis, S. Nam, J. Aumentado, and C. Urbina, *Phys. Rev. Lett.* **89**, 117901 (2002).
8. I. Chiorescu, Y. Nakamura, C. J. P. M. Harmans, and J. E. Mooij, *Science* **299**, 1869 (2003).
9. I. Chiorescu, P. Bertet, K. Semba, Y. Nakamura, C. J. P. M. Harmans, and J. E. Mooij, *Nature* **431** (7005), 159 (2004).
10. A. Wallraff, D. I. Schuster, A. Blais, L. Frunzio, R.-S. Huang, J. Majer, S. Kumar, S. M. Girvin, and R. J. Schoelkopf, *Nature* **431** (7005), 162 (2004).
11. K. J. Boller, A. Imamoglu, and S. E. Harris, *Phys. Rev. Lett.* **66**, 2593 (1991).
12. S. E. Harris, *Phys. Today* **50** (7), 36 (1997).
13. K. V. R. M. Murali, Z. Dutton, W. D. Oliver, D. S. Crankshaw, and T. P. Orlando, *Phys. Rev. Lett.* **93**, 87003 (2004).
14. L. V. Hau, S. E. Harris, Z. Dutton, and C. H. Behroozi, *Nature (London)* **397**, 594 (1999).
15. M. M. Kash, V. A. Sautenkov, A. S. Zibrov, L. Hollberg, G. R. Welch, M. D. Lukin, Y. Rostovtsev, E. S. Fry, and M. O. Scully, *Phys. Rev. Lett.* **82**, 5229 (1999).
16. D. Budker, D. F. Kimball, S. M. Rochester, and V. V. Yashchuk, *Phys. Rev. Lett.* **83**, 1767 (1999).
17. K. Segall, D. Crankshaw, D. Nakada, T. P. Orlando, L. S. Levitov, S. Lloyd, N. Markovic, S. O. Valenzuela, M. Tinkham, and K. K. Berggren, *Phys. Rev. B* **67**, 220506R (2003).
18. D. S. Crankshaw, K. Segall, D. Nakada, T. P. Orlando, L. S. Levitov, S. Lloyd, S. O. Valenzuela, N. Markovic, M. Tinkham, and K. K. Berggren, *Phys. Rev. B* **69**, 144518 (2004).
19. Y. Yu, D. Nakada, J. C. Lee, B. Singh, D. S. Crankshaw, T. P. Orlando, K. K. Berggren, and W. D. Oliver, *Phys. Rev. Lett.* **92**, 117904 (2004).
20. Z. Zhou, S.-I. Chu, and S. Han, *Phys. Rev. B* **66**, 054527 (2002); C.-P. Yang, S.-I. Chu, and S. Han, *Phys. Rev. A* **67**, 042311 (2003).
21. M. H. S. Amin, A. Y. Smirnov, and A. M. van den Brink, *Phys. Rev. B* **67**, 100508R (2003).
22. Z. Kis and E. Paspalakis, *Phys. Rev. B* **69**, 024510 (2004).
23. T. P. Orlando, J. E. Mooij, L. Tian, C. H. van der Wal, L. S. Levitov, S. Lloyd, and J. J. Mazo, *Phys. Rev. B* **60**, 15398 (1999).

24. J. E. Mooij, T. P. Orlando, L. Levitov, L. Tian, C. H. van der Wal, and S. Lloyd, *Science* **285**, 1036 (1999).
25. M. O. Scully and M. S. Zubairy, *Quantum Optics* (Cambridge University Press, Cambridge, 1997).
26. Z. Dutton, Ph.D. thesis, Harvard University, 2002.

7. ADVANCED SILICON TECHNOLOGY

7.1 HIGH-SPEED SCHOTTKY BARRIER pMOSFET WITH $f_T = 280$ GHz

Scaling of traditional CMOS is running into fundamental problems, including high leakage current, shallow junction formation, and high parasitic resistance/capacitance [1],[2]. The control of these issues is leading to increasingly complex fabrication processes that include many precise implant steps with tight thermal budgets. Schottky barrier MOS (SBMOS) offers an alternative device technology in which the source and drain are formed using Schottky barrier contacts, usually implemented with metal silicides [3]–[5]. Platinum silicide is most often used as a low-barrier (0.23 V) pMOS junction while erbium silicide provides a low-barrier (0.28 V) nMOS junction. SBMOS technology offers device scaling with a far simpler fabrication process. For example, no extension or source-drain implants are required since the physical silicide forms the desired junction boundary. Because of the metal silicide source-drain architecture, SBMOS transistors have inherently low parasitic source and drain resistances and high transconductance, making them promising candidates for high-performance RF devices.

A simple four-mask process was used to fabricate bulk-Si Schottky barrier pMOS devices: active, gate, contact, and metal. As shown in Figure 7-1, device isolation was provided using a standard 250-nm recessed local oxidation of silicon (LOCOS) process. An optional 100-keV, 10^{13} -cm $^{-2}$ blanket As implant to the active area was performed on some devices to reduce off-state leakage current. The implant was activated with a 1050°C, 10-s anneal. This leakage suppression implant can be tuned to trade off high current drive against low leakage depending on the device application. The gate stack consisted of a

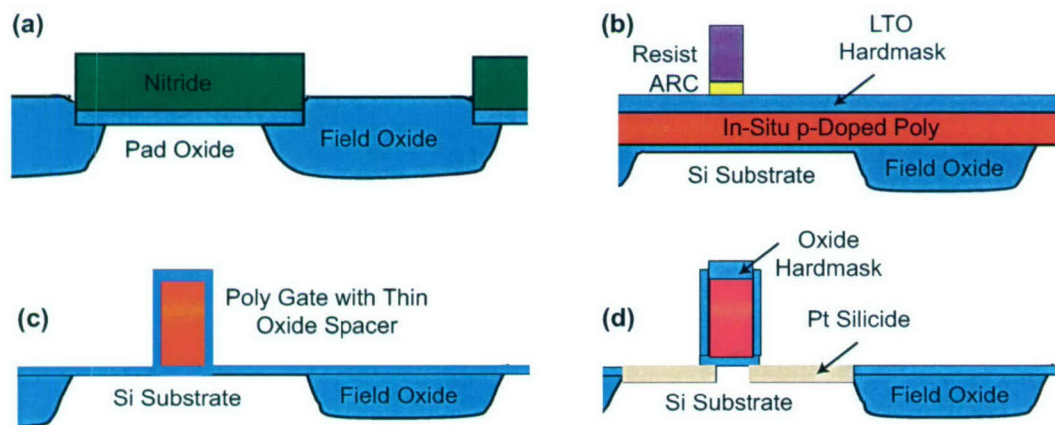


Figure 7-1. Schematic of Schottky barrier transistor fabrication process. (a) LOCOS isolation, (b) gate stack lithography, (c) gate etch and thin oxide spacer formation, and (d) Pt-silicide source drain formation. No implants are used in this process.

100-nm-thick in-situ phosphorus-doped amorphous silicon on a 1.8-nm-thick gate oxide, which is approximately two times thicker than the 0.9-nm equivalent oxide thickness prescribed by the International Technology Roadmap for Semiconductors for devices of this channel length [2]. An n -type gate, instead of the p -type normally desired for pFETs, was used because of our available process limitations. The use of an n -type gate results in a 1.1-V threshold voltage shift as will be shown later. Gate lithography was performed using a 248-nm stepper with a double-exposure phase shift mask approach [6]. An oxide hardmask was used for the gate etch to improve selectivity to the thin gate oxide.

A sub-10-nm oxide was grown on the gate sidewall to act as a thin spacer using an 1100°C, 5-s rapid thermal anneal process, which also provides gate activation. The thin spacer is required to ensure the extension under the gate of the PtSi source and drain Schottky junctions. Devices had minimum gate lengths in the sub-25-nm range. A PtSi salicide process was used to form the silicide source and drain junctions. Platinum was deposited in a molecular beam epitaxy system and annealed in a sinter tube at 550°C for 60 min. Unreacted Pt was stripped in aqua regia to form the self-aligned source-drain contact. Device metallization for probing was performed using an aluminum lift-off process. Figure 7-2 shows scanning electron microscopy and transmission electron microscopy images of a sub-25-nm Schottky pMOS transistor.

Low-leakage sub-25-nm pMOS transistor current-voltage (I-V) curves are shown in Figure 7-3. These devices received a single blanket As implant for leakage current reduction and are the first reported

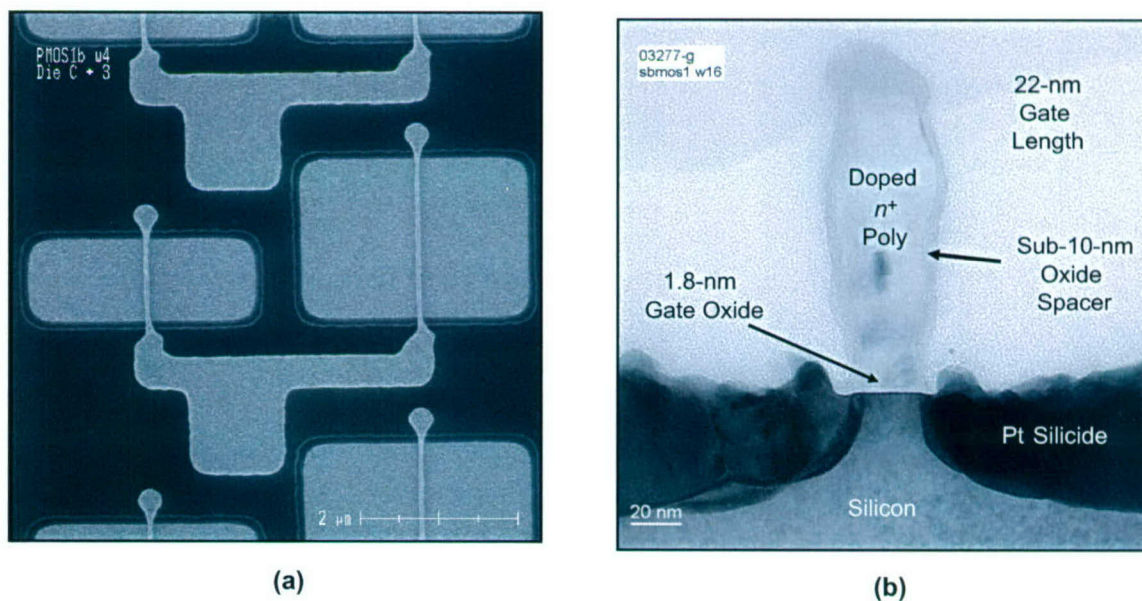


Figure 7-2. Sub-25-nm gate length transistor: (a) Top-down scanning electron micrograph and (b) cross-sectional transmission electron micrograph.

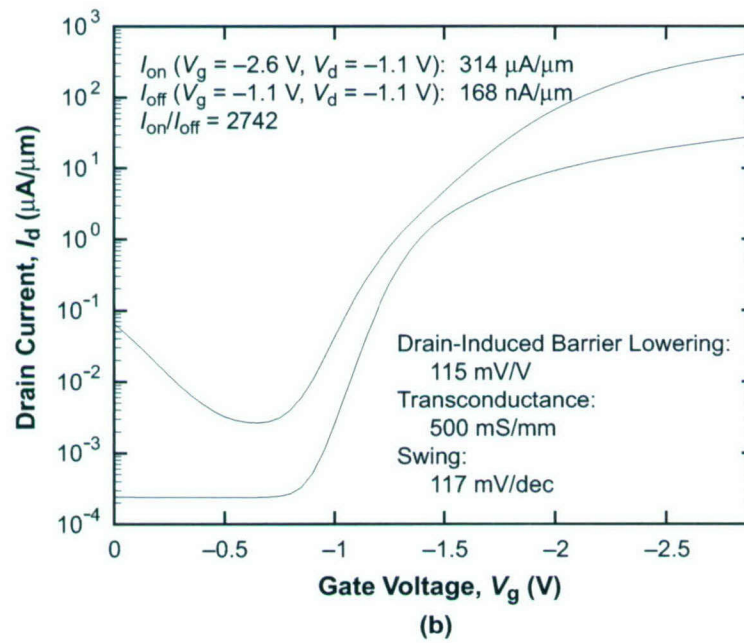
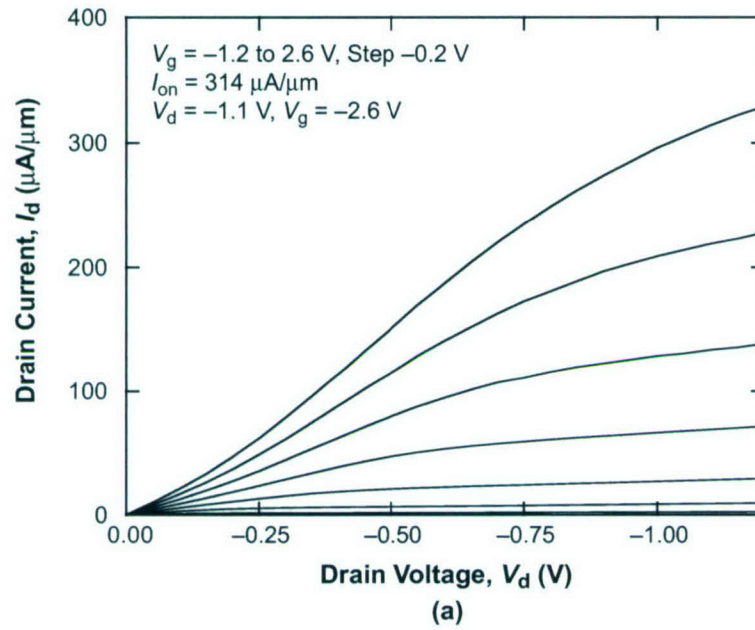


Figure 7-3. (a) Drain current vs drain voltage and (b) drain current vs gate voltage for low-leakage sub-25-nm pMOS transistor. This device received a single blanket As implant for off-state leakage reduction.

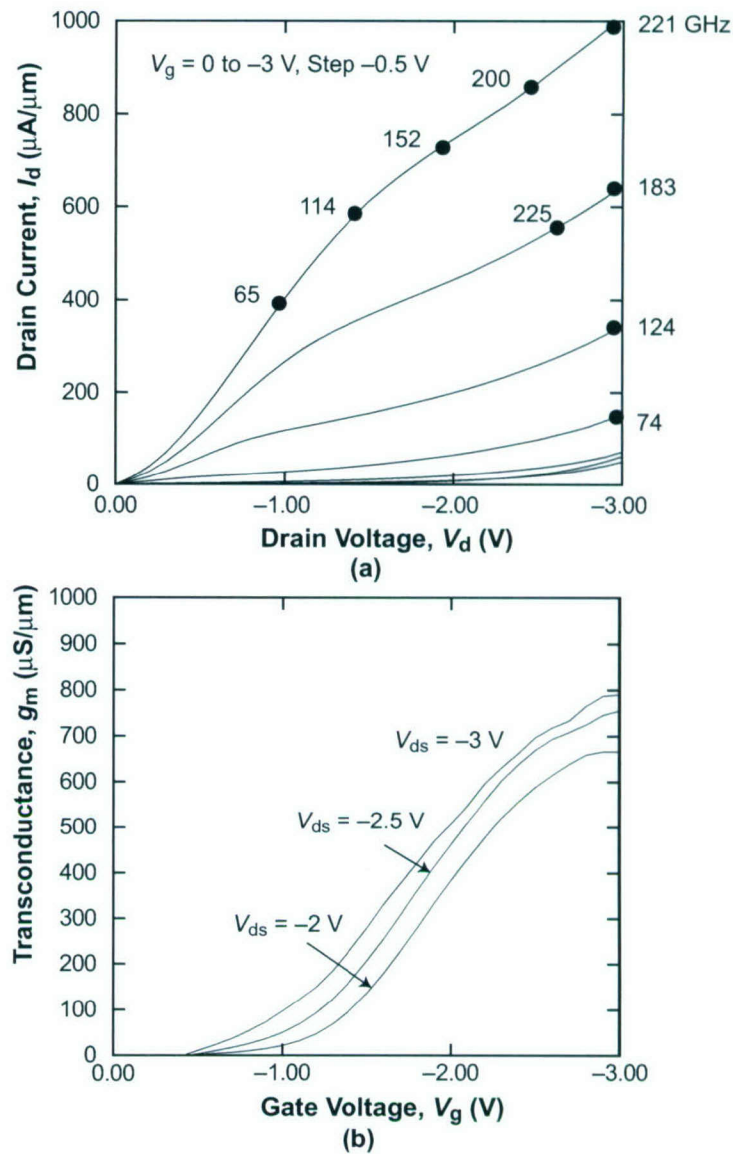


Figure 7-4. (a) Drain current vs drain voltage and (b) transconductance vs gate voltage for pMOS transistor without implants. Values of cutoff frequency (in GHz) as a function of device bias are plotted in (a) next to the solid circles.

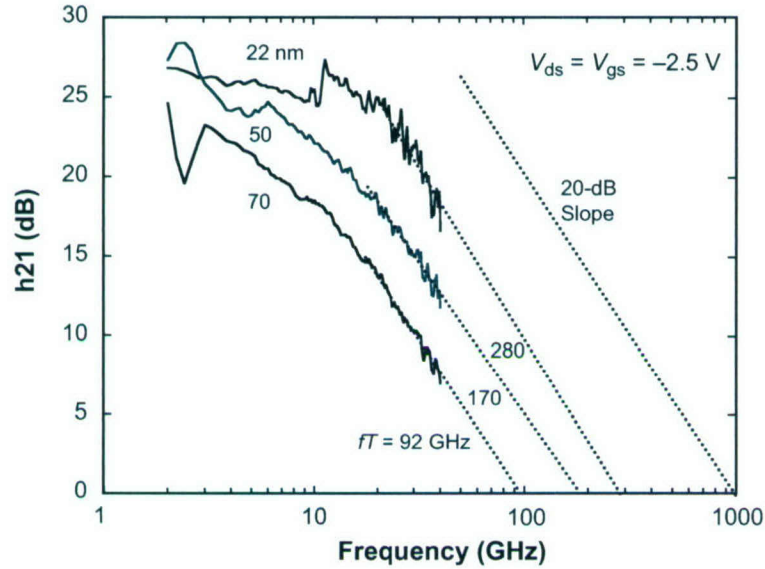


Figure 7-5. RF test results and extrapolated cutoff frequency f_T values for 22-, 50-, and 70-nm gate length pMOS transistors. The S parameters were measured from 2 to 40 GHz.

SBMOS devices having a channel implant. Off-state current was $168 \text{ nA}/\mu\text{m}$ at drain voltage $V_D = -1.1 \text{ V}$ and gate voltage $V_G = -1.1 \text{ V}$, which is equivalent to $V_G = 0 \text{ V}$ if a p -type gate were used. A drive current of $314 \text{ } \mu\text{A}/\mu\text{m}$ was achieved at $V_D = -1.1 \text{ V}$ and $V_G = -2.6 \text{ V}$, providing an $I_{\text{on}}/I_{\text{off}}$ ratio of 1870, the highest reported to date for bulk SBMOS device technology. There is a 1.1-V threshold voltage shift in V_G owing to the use of an n -type gate, and the on-state V_G of -2.6 V provides an electric field in the oxide appropriate for the relatively thick 1.8-nm gate oxide. The upward sloping turn-on in Figure 7-2(a) at low V_D is characteristic of the reverse-biased Schottky barrier diode at the source. The turn-on characteristic is not indicative of high parasitic series resistances for the source and drain regions, which including the contact and source-drain sheet resistances were measured to have a total parasitic series resistance of $\approx 15 \text{ } \Omega \cdot \mu\text{m}$.

Sub-25-nm pMOS transistor results for devices without the As implant are shown in Figure 7-4. A drive current of $324 \text{ } \mu\text{A}/\mu\text{m}$ at $V_D = -1.1 \text{ V}$ and $V_G = -2.6 \text{ V}$ and an off-state current of $6800 \text{ nA}/\mu\text{m}$ were achieved, providing an $I_{\text{on}}/I_{\text{off}}$ ratio of 48. Figure 7-4(b) shows the transconductance g_m of the unimplanted sub-25-nm pMOS device in the overdriven regime. Scattering parameters were measured with on-wafer probes up to 40 GHz using a network analyzer. Probe-pad parasitic capacitance was de-embedded using standard RF calibration procedures. The cutoff frequency f_T values, extrapolated from the $|h_{21}|$ plots shown in Figure 7-5, are 92 and 170 GHz for pMOSFETs with gate lengths of 70 and 50 nm, respectively. The shortest-channel device with sub-25-nm gate length had an extrapolated f_T value of 280 GHz. To the best of our knowledge, this is the highest f_T reported to date for any silicon MOS transistors, including nMOSFETs [7]–[11].

The high f_T values of the SBMOS pFETs can be attributed to high transconductance and low parasitic capacitance of these short-channel devices. Further improvement of RF performance for these devices can be achieved by increasing the relatively low output conductance, shown in Figures 7-3 and 7-4. Several improvements are possible, including an optimized channel implant, reduced effective oxide thickness (EOX), or the use of SOI substrates. Reduced EOX will translate to higher transconductance and potentially further improved f_T performance. Drive current could be further increased by the use of a lower barrier silicide [12] at the expense of higher off-state leakage as well as new materials challenges.

In conclusion, high-speed Schottky barrier pMOS devices with gate lengths less than 30 nm have been fabricated. Even without optimization, an f_T of 280 GHz, the highest for any MOSFET to date, was achieved. SBMOS technology offers promise for RF applications because of high current drive, low parasitic resistance, and simple fabrication. The use of a blanket implant was shown to reduce off-state leakage to values of interest for digital logic applications at a moderate reduction in drive current.

M. Fritze	C. L. Chen	S. Calawa
D. Yost	B. Wheeler	P. Wyatt
C. L. Keast	J. Snyder	J. Larson

REFERENCES

1. Y. Taur, *IBM J. Res. Dev.* **46**, 213 (2002).
2. International Technology Roadmap for Semiconductors
<http://public.itrs.net/Files/2003ITRS/Home2003.htm>
3. J. P. Snyder, C. R. Helms, and Y. Nishi, *Appl. Phys. Lett.* **46**, 1420 (1995).
4. C. Wang, J. P. Snyder, and J. R. Tucker, *Appl. Phys. Lett.* **74**, 1174 (1999).
5. J. Kedzierski, P. Xuan, E. H. Anderson, J. Bokor, T. J. King, and C. Hu, *IEEE Electron Devices Meeting Technical Digest* (IEEE, Piscataway, NJ, 2000), p. 57.
6. M. Fritze, R. Mallen, B. Wheeler, D. Yost, J. P. Snyder, B. Kasprowicz, B. Eynon, and H. Y. Liu, *Proc. SPIE* **5040**, 327 (2003).
7. C-Y. Chang, J. G. Su, H. M. Hsu, S. C. Wong, T. Y. Huang, and Y. C. Sun, *Symposium on VLSI Digest of Technical Papers* (IEEE, Piscataway, NJ, 2001), p. 89.
8. C. H. Diaz, D. D. Tang, and J. Sun, *IEEE Trans. Electron Devices* **50**, 557 (2003).
9. W. Jeamsaksiri, M. Jurczak, L. Grau, D. Linten, E. Augendre, M. De Potter, R. Rooyackers, P. Wambacq, and G. Badenes, *IEEE Trans. Electron Devices* **50**, 610 (2003).
10. J. J. Liou and F. Schwierz, *Solid-State Electron.* **47**, 1881 (2003).

11. H. Momose, E. Morifuji, T. Yoshitomi, T. Ohguro, M. Saito, and H. Iwai, *IEEE Trans. Electron Devices* **48**, 1165 (2001).
12. J. Guo and M. S. Lundstrum, *IEEE Trans. Electron Devices* **49**, 1897 (2002).

REPORT DOCUMENTATION PAGE				Form Approved OMB No. 0704-0188																	
Public reporting burden for this collection of information is estimated to average 1 hour per response, including the time for reviewing instructions, searching existing data sources, gathering and maintaining the data needed, and completing and reviewing this collection of information. Send comments regarding this burden estimate or any other aspect of this collection of information, including suggestions for reducing this burden to Department of Defense, Washington Headquarters Services, Directorate for Information Operations and Reports (0704-0188), 1215 Jefferson Davis Highway, Suite 1204, Arlington, VA 22202-4302. Respondents should be aware that notwithstanding any other provision of law, no person shall be subject to any penalty for failing to comply with a collection of information if it does not display a currently valid OMB control number. PLEASE DO NOT RETURN YOUR FORM TO THE ABOVE ADDRESS.																					
1. REPORT DATE (DD-MM-YYYY) 15-8-2004		2. REPORT TYPE Quarterly Technical Report		3. DATES COVERED (From - To) 1 May - 31 July 2004																	
4. TITLE AND SUBTITLE Solid State Research				5a. CONTRACT NUMBER F19628-00-C-0002																	
				5b. GRANT NUMBER																	
				5c. PROGRAM ELEMENT NUMBER																	
6. AUTHOR(S) David C. Shaver				5d. PROJECT NUMBER 221																	
				5e. TASK NUMBER 961																	
				5f. WORK UNIT NUMBER																	
7. PERFORMING ORGANIZATION NAME(S) AND ADDRESS(ES) Lincoln Laboratory, MIT 244 Wood Street Lexington, MA 02420-9108				8. PERFORMING ORGANIZATION REPORT NUMBER 2004:3																	
9. SPONSORING / MONITORING AGENCY NAME(S) AND ADDRESS(ES) HQ Air Force Materiel Command AFMC/STSC Wright-Patterson AFB, OH 45433-5001				10. SPONSOR/MONITOR'S ACRONYM(S)																	
				11. SPONSOR/MONITOR'S REPORT NUMBER(S) ESC-TR-2005-052																	
12. DISTRIBUTION / AVAILABILITY STATEMENT Approved for public release; distribution is unlimited.																					
13. SUPPLEMENTARY NOTES None																					
14. ABSTRACT This report covers in detail the research work of the Solid State Division at Lincoln Laboratory for the period 1 May through 31 July 2004. The topics covered are Quantum Electronics, Electro-optical Materials and Devices, Submicrometer Technology, Biosensor and Molecular Technologies, Advanced Imaging Technology, Analog Device Technology, and Advanced Silicon Technology. Funding is provided by several DoD organizations—including the Air Force, Army, DARPA, MDA, Navy, NSA, and OSD—and also by the DOE, NASA, and NIST.																					
15. SUBJECT TERMS <table border="0" style="width: 100%;"> <tr> <td>quantum electronics</td> <td>biosensor technology</td> <td>Yb:YAG lasers</td> <td>orthogonal-transfer arrays</td> </tr> <tr> <td>electro-optical devices</td> <td>molecular technology</td> <td>avalanche photodiodes</td> <td>superconductive quantum circuits</td> </tr> <tr> <td>materials research</td> <td>advanced imaging technology</td> <td>InGaAsP growth</td> <td>pMOSFETs</td> </tr> <tr> <td>submicrometer technology</td> <td>analog device technology</td> <td>optical lithography</td> <td></td> </tr> </table>						quantum electronics	biosensor technology	Yb:YAG lasers	orthogonal-transfer arrays	electro-optical devices	molecular technology	avalanche photodiodes	superconductive quantum circuits	materials research	advanced imaging technology	InGaAsP growth	pMOSFETs	submicrometer technology	analog device technology	optical lithography	
quantum electronics	biosensor technology	Yb:YAG lasers	orthogonal-transfer arrays																		
electro-optical devices	molecular technology	avalanche photodiodes	superconductive quantum circuits																		
materials research	advanced imaging technology	InGaAsP growth	pMOSFETs																		
submicrometer technology	analog device technology	optical lithography																			
16. SECURITY CLASSIFICATION OF:			17. LIMITATION OF ABSTRACT None	18. NUMBER OF PAGES 68	19a. NAME OF RESPONSIBLE PERSON																
a. REPORT Unclassified	b. ABSTRACT Same as report	c. THIS PAGE Same as report			19b. TELEPHONE NUMBER (include area code)																